Constraints on the Physical Origin of Large Cavities in Transition Disks from Multiwavelength Dust Continuum Emission

Anibal Sierra, Laura M. Pérez, Benjamín Sotomayor, Myriam Benisty, Claire J. Chandler, Sean Andrews, John Carpenter, Thomas Henning, Leonardo Testi, Luca Ricci, et al.

The Astrophysical Journal, 974:306 (19pp), 2024 October 20 https://doi.org/10.3847/1538-4357/ad7460

Constraints on the Physical Origin of Large Cavities in Transition Disks from Multiwavelength Dust Continuum Emission

Anibal Sierra[1,2], Laura M. Pérez[1], Benjamín Sotomayor[1], Myriam Benisty[3,4], Claire J. Chandler[5], Sean Andrews[6], John Carpenter[7], Thomas Henning[8], Leonardo Testi[9,10], Luca Ricci[11], and David Wilner[6]
[1] Departamento de Astronomía, Universidad de Chile, Camino El Observatorio 1515, Las Condes, Santiago, Chile; anibalsierram@gmail.com
[2] Instituto de Astrofísica, Pontificia Universidad Católica de Chile, Av. Vicuña Mackenna 4860, 7820436 Macul, Santiago, Chile
[3] Univ. Grenoble Alpes, CNRS, IPAG, 38000 Grenoble, France
[4] Université Côte d'Azur, Observatoire de la Côte d'Azur, CNRS, Laboratoire Lagrange, France
[5] National Radio Astronomy Observatory, P.O. Box O, Socorro, NM 87801, USA
[6] Center for Astrophysics | Harvard & Smithsonian, Cambridge, MA 02138, USA
[7] Joint ALMA Observatory, Avenida Alonso de Córdova 3107, Vitacura, Santiago, Chile
[8] Max-Planck-Institut für Astronomie (MPIA), Königstuhl 17, 69117 Heidelberg, Germany
[9] Alma Mater Studiorum Università di Bologna, Dipartimento di Fisica e Astronomia (DIFA), Via Gobetti 93/2, 40129 Bologna, Italy
[10] INAF –Osservatorio Astrofisico di Arcetri, Largo E. Fermi 5, 50125 Firenze, Italy
[11] Department of Physics and Astronomy, California State University Northridge, 18111 Nordhoff Street, Northridge, CA 91330, USA
Received 2024 April 9; revised 2024 August 26; accepted 2024 August 26; published 2024 October 18

Abstract

The physical origin of the large cavities observed in transition disks is to date still unclear. Different physical mechanisms (e.g., a companion, dead zones, enhanced grain growth) produce disk cavities of different depth, and the expected spatial distribution of gas and solids in each mechanism is not the same. In this work, we analyze the multiwavelength interferometric visibilities of dust continuum observations obtained with Atacama Large Millimeter/submillimeter Array and Very Large Array for six transition disks: CQTau, UXTau A, LkCa15, RXJ1615, SR24S, and DMTau, and calculate brightness radial profiles, where diverse emission morphology is revealed at different wavelengths. The multiwavelength data are used to model the spectral energy distribution and compute constraints on the radial profile of the dust surface density, maximum grain size, and dust temperature in each disk. They are compared with the observational signatures expected from various physical mechanisms responsible for disk cavities. The observational signatures suggest that the cavities observed in the disks around UXTau A, LkCa15, and RXJ1615 could potentially originate from a dust trap created by a companion. Conversely, in the disks around CQTau, SR24S, DMTau, the origin of the cavity remains unclear, although it is compatible with a pressure bump and grain growth within the cavity.

Unified Astronomy Thesaurus concepts: Protoplanetary disks (1300); Circumstellar dust (236); Millimeter astronomy (1061); Submillimeter astronomy (1647); Radio interferometry (1346)

1. Introduction

Protoplanetary disks are dynamic objects. Physical processes, such as photoevaporation (e.g., R. D. Alexander et al. 2006), accretion (e.g., L. Hartmann et al. 2016), dust migration and segregation (e.g., F. L. Whipple 1972; S. J. Weidenschilling 1977; T. Takeuchi & D. N. C. Lin 2002), dust growth (e.g., L. Testi et al. 2014; T. Birnstiel et al. 2016), settling (e.g., R. Schräpler & T. Henning 2004; H. Avenhaus et al. 2018; E. A. Rich et al. 2021), and disk winds (A. Konigl & R. E. Pudritz 2000; I. Pascucci et al. 2023), are taking place in protoplanetary disks. These mechanisms have an important impact on the disk evolution, the spatial distribution of solids and gas, and thus, on the observed disk morphologies at different wavelengths.

In the last decade, high angular resolution observations of protoplanetary disks have unveiled a diversity of large and small spatial scale substructures, including vortices (e.g., J. M. Brown et al. 2009; S. M. Andrews et al. 2009; S. Casassus et al. 2013; L. M. Pérez et al. 2014; C. M. T. Robert et al. 2020; J. Varga et al. 2021), cavities (e.g., L. Francis & N. van der Marel 2020), rings and gaps (e.g., J. Huang et al. 2018), spiral arms (e.g., D. Mouillet et al. 2001; T. Muto et al. 2012; L. M. Pérez et al. 2016; T. Paneque-Carreño et al. 2021), and circumplanetary disks (A. Isella et al. 2019b; M. Benisty et al. 2021; V. Christiaens et al. 2024). The origin of the observed morphologies has been attributed to various physical mechanisms such as gravitational instabilities (A. Toomre 1964), magnetorotational instability (S. A. Balbus & J. F. Hawley 1991), dust traps (F. L. Whipple 1972; H. H. Klahr & T. Henning 1997), planet–disk interactions (e.g., D. N. C. Lin & J. Papaloizou 1979; P. Goldreich & S. Tremaine 1979), and snow lines (e.g., C. Hayashi 1981), among others.

The existence of large dust cavities (with sizes from a few astronomical units to hundreds of astronomical units, L. Francis & N. van der Marel 2020) in the so-called "transition disks" was first inferred by near-infrared observations (K. M. Strom et al. 1989), and then by their millimeter spectral energy distribution (SED; N. Calvet et al. 2002), long before high angular resolution data became available. The SED of these objects shows an excess emission at millimeter wavelengths, but no excess emission at mid-infrared wavelengths. This distinct signature was initially interpreted as a deficit of hot material in the inner disk region (e.g., K. M. Strom et al. 1989; N. Calvet et al. 2002; J. M. Brown et al. 2007), an interpretation that was later confirmed through subsequent

high angular resolution observations (S. M. Andrews et al. 2011).

The physical origin of large cavities in transition disks remains unclear. Nonetheless, various proposed mechanisms aim to replicate these observed dust cavities. As pointed out by N. van der Marel (2023), these mechanisms include the presence of companions (P. Artymowicz & S. H. Lubow 1996), dead zones (Z. Regály et al. 2012; M. Flock et al. 2015), photoevaporation (R. D. Alexander et al. 2006; M. Gárate et al. 2021), and/or grain growth (C. P. Dullemond et al. 2001). In scenarios involving companions, an already formed planet or a close binary can carve a significant gap in the disk, inhibiting the radial migration of dust grains and resulting in the formation of a large cavity (e.g., R. Dong et al. 2015). This mechanism leads to the creation of a dust trap at the outer edge of the cavity due to the pressure gradient (P. Pinilla et al. 2012a).

A large cavity can also form by a dead zone, where the particle flow halts due to a jump in gas surface density and a pressure maximum (M. Flock et al. 2015). Unlike the mechanism involving a companion, the dead zone scenario does not predict a gas gap within the cavity (P. Pinilla et al. 2016).

On the other hand, dust cavities can also form via dust growth. In this mechanism, large grains are expected to have a fast radial migration toward the inner region of the disk (T. Takeuchi & D. N. C. Lin 2002), resulting in a deficit of dust mass within the disk cavity. Additionally, very large grains (with sizes exceeding about 1 cm) have a low opacity at millimeter wavelengths (e.g., B. T. Draine 2006), thereby reducing the dust continuum emission within the cavity. However, even in the most optimistic scenario where dust growth is very efficient, this mechanism alone has been shown to be insufficient for creating large cavities within 5 Myr of dust evolution (T. Birnstiel et al. 2012a). Thus, in addition to dust growth, another physical mechanism producing a pressure bump is needed to reproduce the significant drop of millimeter emission within the cavities of transition disks (T. Birnstiel et al. 2012a).

Different observational signatures are expected depending on whether the large cavities result from a companion, dead zone, photoevaporation, or enhanced grain growth. In scenarios involving a dust trap (created by a companion or a dead zone), one would expect an increase in both surface density and maximum grain size at the outer border of the cavity. Conversely, if enhanced grain growth and a pressure bump are responsible for the large cavity, we would expect to infer a prevalence of large dust grains in the inner region of the disk and dust grains being trapped at the border of the cavity.

Observational constraints on the dust surface density, maximum grain size, and temperature can offer valuable insights into the origin of cavities within transition disks. Fortunately, these constraints can be derived from polarized observations (A. Kataoka et al. 2016a, 2016b; H. Yang et al. 2016, 2024; Z.-Y. D. Lin et al. 2024) or from fitting the SED of the dust continuum emission (e.g., L. M. Pérez et al. 2012; C. Carrasco-González et al. 2019; A. Sierra et al. 2021; E. Macías et al. 2021; H. B. Liu et al. 2024). It is known that both methodologies offer different grain size estimations (hundreds for microns from polarization and a few millimeters from the SED). Although some works (R. Tazaki et al. 2019; S. Zhang et al. 2023; Z.-Y. D. Lin et al. 2023) have demonstrated that millimeter porous grains can help to alleviate the tension, it has been shown that only the opacity of compact dust grains can reproduce the observed spectral index in disk population synthesis (L. Delussu et al. 2024).

Table 1
Stellar and Disk Properties

Source	Distance (pc)	i (deg)	PA (deg)	L_* ($L_\odot$)	M_* ($M_\odot$)
CQTau	149.4	36.3	46.5	10.0	1.63
UXTau	140	40.9	168.7	2.5	1.4
LkCa15	157.2	49.7	62.1	1.3	1.32
RXJ1615	155.6	46.9	146.1	1.3	1.1
SR24S	114	47.8	26.6	2.5	0.87
DMTau	144.0	35.7	157.1	0.2	0.39

Note. References: Inclination and geometry are computed in this work. The distances are taken from Gaia Collaboration (2020), and the luminosity and mass of the star from A. Natta et al. (2006), C. Espaillat et al. (2010), Z. Wahhaj et al. (2010), S. M. Andrews et al. (2011), C. F. Manara et al. (2014), N. van der Marel et al. (2015), M. G. Ubeira Gabellini et al. (2019), and L. Francis & N. van der Marel (2020).

In this paper, we analyze the dust continuum emission of six known transition disks: CQTau, UXTau A, LkCa15, RXJ1615, SR24S, and DMTau, with cavity sizes of approximately 50, 31, 76, 30, 35, and 25 au, respectively (P. Pinilla et al. 2014; L. Francis & N. van der Marel 2020). One of the goals of this work is to compare the multiwavelength brightness profile for each disk, and infer dust properties that can provide insights into the origin of the cavities.

The observational data are presented in Section 2. The analysis and modeling of dust continuum visibilities for each observation are conducted in Section 3, where high angular resolution radial profiles are computed from the data. Section 4 presents the analysis of multiwavelength radial profiles, revealing constraints on the dust surface density, maximum grain size, and dust temperature within each disk. The discussion of the physical mechanisms influencing each disk is outlined in Section 5, and the general properties are discussed in Section 6, followed by conclusions in Section 7.

2. Observations

We used 26 archival dust continuum observations of six transition disks: CQ Tau, UX Tau, LkCa15, RXJ1615, SR24S, and DMTau. The dust continuum observations span from optically thick emission (observed in Atacama Large Millimeter/submillimeter Array, hereafter ALMA, Band 9 or Band 7) to optically thin emission (observed in Very Large Array, hereafter VLA, Band Q or Band Ka) in all disks, with beam sizes of tens and hundreds of milliarcseconds. The distance, stellar parameters, and geometry in each disk are summarized in Table 1. A summary of the multiwavelength data sets, final imaging properties, and project codes for both ALMA and VLA observations can be found in Table 2, and there is a gallery of the dust continuum images in Figure 1.

The ALMA data were self-calibrated using CASA 6.4.3.27. All spectral windows and scans are combined to improve the signal-to-noise ratio (SNR) using `combine='spws, scans'` within the CASA `gaincal` task. We began applying phase self-calibration with an initial solution time interval equal to the total observation time. The new self-calibrated data were imaged, and the SNR is computed. If SNR improves by at least

Table 2
Properties of the Millimeter Continuum Images

Source	ALMA/VLA Band	ν (GHz)	Baselines (m–km)	On-source Time (minutes)	Robust	Synthesized Beam (mas×mas; deg)	rms Noise (μJy beam^{-1})	ALMA/VLA Project Code
CQTau	7	338	21–0.4	22.1	0.5	674 × 469; 15	530.0	2011.0.00320.S
	6	225	3–8.5	93.2	0.5	267 × 231; –16	35.0	2013.1.00498.S
	Ka	34	80–11.1	115.1	2.0	401 × 293; 61	7.7	AC982
UXTau A	7	344	16–1.5	54.4	0.5	193 × 151; –22	49.0	2015.1.00888.S
	6	232	15–1.6	14.1	0.5	253 × 209; 11	37.3	2013.1.00498.S
	3	96	18–7.6	8.6	0.5	296 × 140; 49	27.0	2016.1.01042.S
	Q	42	78–11.1	144.2	2.0	315 × 235; –57	14.9	AC982
LkCa15	9	689	21–0.4	17.1	0.5	306 × 229; –35	1650.0	2011.0.00724.S
	7	340	34–8.5	162.1	0.5	47 × 27; 23	16.5	2018.1.00350.S
	6	229	15–12.7	140.2	0.5	84 × 57; –30	14.4	2018.1.01255.S
	Q	44	78–27.9	1129.0	2.0	149 × 144; 64	4.2	AC982,13B-381,12B-196
RXJ1615	9	689	21–0.4	22.2	0.5	288 × 193; –80	1750.0	2011.0.00724.S
	7	339	18–3.7	59.4	0.5	73 × 61; 84	28.0	2012.1.00870.S
	Q	44	243–11.1	152.4	2.0	498 × 294; –17	16.2	13B-381
SR24S	9	689	21–0.4	25.2	0.5	368 × 190; –78	1910.0	2011.0.00724.S
	7	337	15–1.6	2.0	0.5	183 × 155; 61	367.1	2013.1.00157.S
	6	231	15–1.6	21.7	0.5	222 × 192; 51	67.1	2013.1.00091.S
	3	109	19–9.5	7.2	0.5	233 × 155; 61	33.4	2016.1.01042.S
	Ka	34	78–36.6	327.5	2.0	180 × 148; 31	7.7	AC982
DMTau	9	676	15–0.5	79.9	0.5	309 × 287; –11	674	2016.1.00565.S
	8	480	15–1.1	11.1	0.5	150 × 115; –6	660	2015.1.01137.S
	7	318	15–0.9	79.5	0.5	455 × 366; 7	139	2016.1.00565.S
	6	232	15–15.2	134.3	0.5	32 × 21; 33	8.4	2018.1.01755.S
	4	145	15–1.1	2.0	0.5	546 × 448; 24	84	2015.1.00296.S
	3	109	19–7.6	8.6	0.5	296 × 158; 48	27	2016.1.01042.S
	Q	42	78–22,814	378.3	2.0	259 × 173; –65	9.0	AC982

a factor of 5%, we continue applying successive phase self-calibration iterations with a smaller solution time interval (it decreases by a factor of 3 in consecutive iterations). Throughout each self-calibration step, we utilized `applymode='calonly'` to calibrate data only, and do not apply flags from solutions. A final amplitude self-calibration iteration with an infinitive solution time interval (`solint='inf'`) and combining spectral windows and scans (`combine='spws,scans'`) is also applied to the data. The calibrated VLA data were taken from the Disks@EVLA Collaboration.[12] The calibration process for the Disks@EVLA data is provided in Section 2.2 of L. M. Pérez et al. (2015) or Section 2 of S. M. Andrews et al. (2014). For imaging, we employed the TCLEAN task with a multiscale CLEAN algorithm with scales corresponding to point sources, 1, 2, and 3 times the beam full width at half-maximum (FWHM). Additionally, we applied a mask covering the disk emission.

3. Visibility Modeling

We fit the deprojected continuum visibilities of the dust continuum emission to extract the highest angular resolution from the observational data. The deprojection of the visibilities is done using the FRANKENSTEIN tools[13] in J. Jennings et al. (2020), where the geometric projecting effects due to the orientation of the interferometer's baselines are corrected. The deprojection consists of rotating the baseline coordinates using the disk's position angle (PA), and then stretching the baseline coordinates along the minor axis of the disk using the cosine of the disk inclination.

We assume azimuthal emission symmetry, which is a first order approximation of the disk morphologies in this work, as shown in Figure 1, although it is known that some of these disks present some degree of azimuthal asymmetry (e.g., DMTau Band *Q* observations in J. Hashimoto et al. 2021).

The interferometric visibilities (which for a given uv-distance, corresponds to the real and imaginary part of the visibility and its associated weight) are extracted from the self-calibrated measurement sets using a modified version from the *export_uvtable* function in M. Tazzari (2017). In our version, the uv-distances are normalized using the wavelength of each channel and spectral window, instead of the average wavelength of the whole data set. The visibility modeling is done using a nonparametric fit (Section 3.1) for observations with high SNR, and with a parametric model for low SNR observations (Section 3.2). In both cases, constraints to the phase shift and geometry of each observation (Section 3.3) are necessary when deprojecting and fitting the visibilities.

3.1. Nonparametric Fit

The nonparametric visibility modeling is performed using FRANKENSTEIN (J. Jennings et al. 2020), where the disk brightness (represented as a Fourier–Bessel series) is reconstructed by fitting the real part of the visibilities as a function of the uv-distance (baselines). The imaginary part of the visibilities, which mainly traces the emission from nonsymmetric structures,

[12] https://safe.nrao.edu/evla/disks/
[13] Available at https://github.com/discsim/frank.

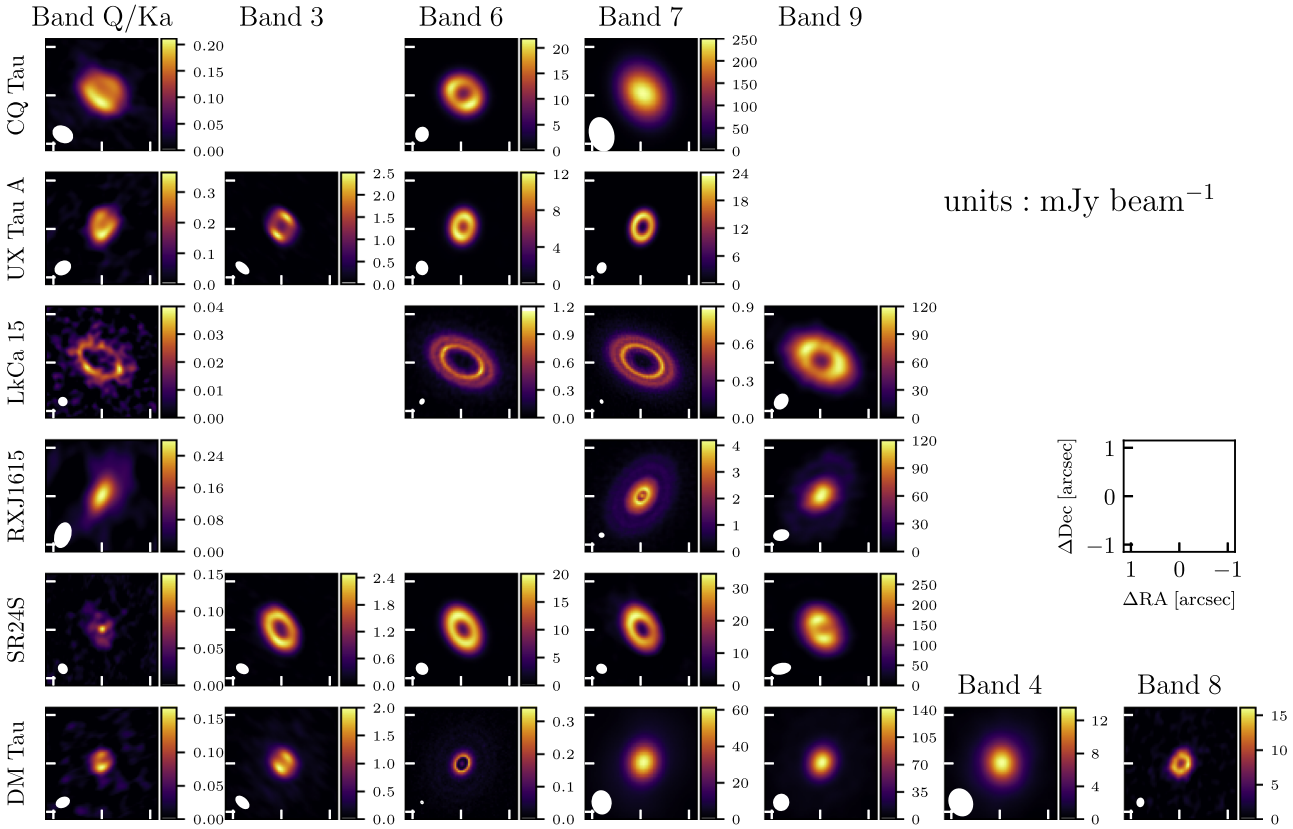

Figure 1. ALMA (from Band 3 to Band 9) and VLA (Band *Q* or Band *Ka*) continuum maps of the six transition disk in our sample. The beam size is shown in the bottom left corner of each panel. xticks and yticks in all panels are separated by 1″.

is not used by FRANKENSTEIN given the azimuthal symmetry assumption (the imaginary part of the visibilities in our observations tends to be zero when averaged over all orientations).

The reconstructed radial profile depends on two hyperparameters: α, $w_{\rm smooth}$. The former mimics the SNR threshold below which the data are not used when fitting the visibilities, and the latter controls the smoothness of the fit to the power-spectrum (see full details about the visibility fit in J. Jennings et al. 2020, 2022).

These hyperparameters do not have strong effects on the reconstructed brightness profiles for disks with a high SNR; however, this is not the case for low SNR data, where a particular combination of α, $w_{\rm smooth}$ can imprint oscillatory artifacts on the reconstructed brightness profile. For this reason, we fit all the observations using a grid of hyperparameters varying between $\alpha = [1.05–1.30]$, and $\log_{10}(w_{\rm smooth}) = [-4, -1]$, and we choose by visual inspection the pair of hyperparameters that minimize the oscillatory artifacts.

The longest wavelengths in our sample (Band *Q* and *Ka* from VLA) have a low SNR at all uv-distances. Thus, for these long wavelength observations, we use FRANKENSTEIN on the binned visibilities (bin size of 10 kλ).

The chosen hyperparameters for each data set are summarized in Table 3. Additional fit parameters (e.g., maximum fitting radius, number of radial points to sample the radial profile) have no important effects on the reconstructed brightness profile if the recommendations described in J. Jennings et al. (2020) are taken into account. We fit the data in the logarithmic brightness space, which helps to reduce the oscillatory artifacts in the reconstructed brightness profile, and prevents negative values in the reconstructed brightness profile. However, we found no important differences when fitting the data in a linear brightness space.

3.2. Parametric Fit

The FRANKENSTEIN models for VLA data were computed by binning the visibilities. Since this procedure results in information loss, we also directly fit the nonbinned VLA visibilities using a parametric model with a given intensity profile $I(r)$. The visibilities of the parametric model are computed using a Hankel transform $\mathcal{H}$ (T. J. Pearson 1999):

$$V(q) = \mathcal{H}(I(r)) = 2\pi \int_0^\infty I(r) J_0(2\pi q r) dr, \quad (1)$$

where r is the disk radius, J_0 is the zeroth-order Bessel function of the first kind, $q = \sqrt{u^2 + v^2}/\lambda$ is the deprojected baseline, λ is the wavelength, and u, v are the coordinates of the baseline vectors.

For each disk, the morphology of the parametric models is motivated by the brightness distribution inferred at ALMA wavelengths with FRANKENSTEIN (an extended discussion on the disk morphology is done for each particular disk in Section 5). We also consider other physical processes that can contribute to the emission at VLA wavelengths, as free–free emission from ionized gas. However, we assume that the emission from spinning nanometer-size dust (T. Hoang et al. 2018) does not contribute to the observed emission, as scattering properties (taken into account in this work) can mimic similar effects to those expected from spinning dust

Table 3
Visibility Modeling Parameters

Source	Band	α	$\log_{10}(w_s)$	i[a] (deg)	PA[a] (deg)	ChanWidth (MHz)	Centering Methodology	Resolution (mas)	Multiwave Analysis
CQTau	7	1.3	−1	$37.9^{+0.5}_{-0.3}$	$46.7^{+1.8}_{-0.1}$	29	Min vis scatter	255.3	No
	6	1.3	−4	$36.3^{+0.1}_{-0.6}$	$46.5^{+0.9}_{-0.4}$	500	Gaussian fit	149.6	Yes
	Ka	1.05	−4	⋯	⋯	128	Gaussian fit	238.4	Yes
UXTau A	7	1.05	−1	$41.9^{+0.5}_{-0.1}$	$168.0^{+0.1}_{-0.5}$	500	Min vis scatter	75.1	Yes
	6	1.3	−1	$41.9^{+0.1}_{-0.7}$	$166.6^{+0.8}_{-0.2}$	117	Min vis scatter	136.5	Yes
	3	1.05	−4	$40.9^{+0.6}_{-0.1}$	$168.7^{+1.0}_{-0.5}$	500	Min vis scatter	112.3	Yes
	Q	1.05	−4	⋯	⋯	128	Gaussian fit	157.0	Yes
LkCa15	9	1.2	−4	$50.8^{+0.2}_{-0.8}$	$61.7^{+2.0}_{-0.1}$	375	Min vis scatter	171.9	No
	7	1.3	−1	$50.5^{+0.1}_{-0.5}$	$61.6^{+0.1}_{-0.2}$	250	Min vis scatter	17.7	Yes
	6	1.3	−1	$49.7^{+0.1}_{-0.2}$	$62.1^{+0.4}_{-0.1}$	250	Min vis scatter	21.5	Yes
	Q	1.05	−4	⋯	⋯	128	Gaussian fit	120.0	Yes
RXJ1615	9	1.05	−4	$40.6^{+9.2}_{-0.9}$	$150.0^{+0.1}_{-5.0}$	375	Min vis scatter	191.4	No
	7	1.3	−1	$46.9^{+0.1}_{-0.9}$	$146.1^{+0.6}_{-0.1}$	235	Min vis scatter	34.2	Yes
	Q	1.05	−4	⋯	⋯	128	Gaussian fit	167.0	Yes
SR24S	9	1.3	−1	$48.7^{+0.2}_{-0.6}$	$27.2^{+0.1}_{-0.5}$	375	Gaussian fit	157.2	No
	7	1.3	−1	$48.6^{+0.1}_{-0.2}$	$27.3^{+0.1}_{-0.3}$	16	Gaussian fit	118.2	Yes
	6	1.3	−1	$47.8^{+0.1}_{-0.1}$	$26.6^{+0.1}_{-0.6}$	469	Gaussian fit	117.2	Yes
	3	1.3	−1	$44.8^{+2.4}_{-0.1}$	$25.1^{+4.0}_{-0.3}$	63	Gaussian fit	98.6	Yes
	Ka	1.05	−4	⋯	⋯	128	Gaussian fit	120.1	Yes
DMTau	9	1.05	−4	$36.6^{+0.1}_{-0.3}$	$156.3^{+0.1}_{-1.1}$	234	Min vis scatter	204.0	No
	8	1.05	−1	$39.9^{+0.4}_{-9.3}$	$153.3^{+4.9}_{-7.3}$	125	Min vis scatter	111.9	Yes
	7	1.3	−1	$40.1^{+1.8}_{-4.7}$	$153.1^{+0.9}_{-4.2}$	63	Min vis scatter	153.8	No
	6	1.3	−1	$35.7^{+0.1}_{-0.1}$	$157.1^{+0.4}_{-0.1}$	469	Min vis scatter	14.2	Yes
	4	1.1	−1	$32.7^{+0.1}_{-0.6}$	$156.0^{+0.2}_{-6.9}$	63	Min vis scatter	273.4	No
	3	1.3	−1	$34.8^{+2.6}_{-0.6}$	$155.2^{+0.5}_{-4.9}$	63	Min vis scatter	72.8	Yes
	Q	1.1	−4	⋯	⋯	128	Gaussian fit	69.6	Yes

Note.
[a] The inferred inclination (i) and position angle (PA) for each observation are reported in this table. However, both values are fixed to those summarized in Table 1 during the visibility modeling.

(A. Sierra & S. Lizano 2020), making it difficult to differentiate between the two processes.

The free–free emission is modeled by including a compact emission point source at the disk center, simulating the expected compact free–free emission at these long wavelengths reported by previous centimeter observations of UXTau A, LkCa15, RXJ1615, and SR24S in L. A. Zapata et al. (2017). For DMTau, no compact free–free emission was detected in L. A. Zapata et al. (2017); however, Y. Terada et al. (2023) found that the free–free emission from ionized gas in DMTau is variable. We include the free–free component in all disks, and then, we compare its inferred flux with previous estimations in Appendix B.2.

The parameter space of the free parameters describing the parametric fit is explored using a Markov Chain Monte Carlo (MCMC; implemented in the Python library EMCEE, D. Foreman-Mackey et al. 2013). The best-fit parametric model is found by maximizing the logarithm of the likelihood function, given by

$$\ln \mathcal{L} = -\frac{1}{2}\sum_j W_j[(\mathrm{ReV}_j^{\mathrm{obs}} - \mathrm{ReV}_j^{\mathrm{mod}})^2 + (\mathrm{ImV}_j^{\mathrm{obs}} - \mathrm{ImV}_j^{\mathrm{mod}})^2], \quad (2)$$

where W_j are the weights of the visibilities, and V_j^{obs}, V_j^{model} are the observed and model visibilities, respectively.

3.3. Phase Shift and Geometry

The offset of the disk center with respect to the phase center (δR.A., δdecl.), disk inclination (i), and disk PA are fitted for each observation.

In most of the cases, the offset is computed by minimizing the imaginary part of the visibilities (e.g., A. Isella et al. 2019a). However, in some cases (e.g., SR24S with some small azimuthal asymmetries), the obtained phase shift does not match with the disk center (visual inspection); thus, in a few cases, we fit a 2D Gaussian function (in the image plane) using a very low angular resolution image (using the UVTAPER task in CASA), where the azimuthal asymmetry vanishes. The methodology used for each observation is summarized in Table 3.

The disk inclination and PA are fitted by minimizing the spread of the deprojected visibilities for circular annuli in the visibility space (e.g., A. Isella et al. 2019a). Error bars are computed from the percentiles 16th and 84th. The inferred disk inclination for a certain disk is consistent within the error bars. However, variations can also occur because disks are not

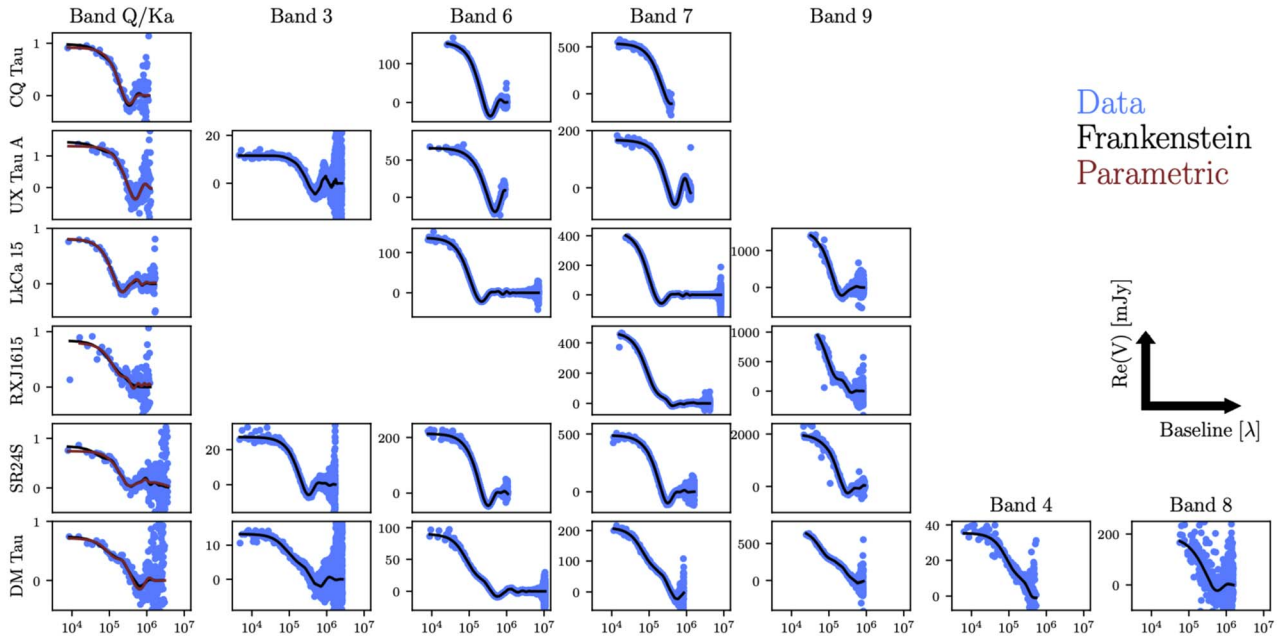

Figure 2. Real part of the dust continuum visibilities (blue points) as a function of baseline for each observation in this work. The black/red solid line is the FRANKENSTEIN/parametric visibility model.

perfectly settled to the midplane, depending on factors such as grain size and turbulent state (e.g., B. Dubrulle et al. 1995; R. Schräpler & T. Henning 2004). Additionally, the contribution of the upper layers becomes more significant at smaller wavelengths (e.g., A. Sierra et al. 2019).

The inferred disk geometry for all the ALMA observations are summarized in Table 3. The geometry derived from the VLA data is poorly constrained and is not included in this table.

One of the goals in this paper is to compare the brightness radial profiles using multiwavelength observations of each disk. For this reason, the geometry of each disk is fixed for all wavelengths. The chosen disk geometry is based on the following criteria: (1) The contribution from the disk midplane should be important (long wavelengths where the emission is optically thin are good candidates). (2) The angular resolution (or uv-distances) should be good enough to resolve the disk geometry. (3) There is high SNR (i.e., the disk geometry is well constrained). The latter discards the Band *Q* and *Ka* observations, where the geometry is poorly constrained. Thus, our final decision on the disk geometry is based on Band 6, 3, 6, 7, 6, 6, for CQTau, UXTau A, LkCa15, RXJ1615, SR24S, and DMTau, respectively.

3.4. Results from the Visibility Modeling

Figure 2 shows the visibility modeling results for the observations in our sample. In all cases, the axisymmetric visibility model (from Frankenstein or parametric) is a good representation of the observed visibilities. Note that the *uv*-coverage of each observation is diverse. For example, for LkCa15, the maximum baseline for Band 6 and 7 is close to 10Mλ, but for Band 9, it is close to 1Mλ. This limits the disk substructures that can be inferred from observations.

Figure 3 shows the normalized brightness radial profile for each observation from the visibility fit and from the image plane. The radial profiles in the image plane were computed using GOFISH (R. Teague 2019) and the same offset and disk geometries as in the visibility fits. We assume a filling factor (A. R. Thompson et al. 2017) of 1 everywhere. This assumption is valid at large radius, where the solid angle of concentric rings is larger than that of the beam size. However, in the most inner region ($\lesssim$50 mas), the radial profiles from the image plane would need a filling factor correction. Nevertheless, the radial profiles from the image plane are only used to visualize the differences compared with the radial profiles computed from the visibility fit, and they are not used in the rest of the manuscript.

The error bars ($\Delta_{\rm img}$) in the radial profile from the image plane ($I_{\rm img}$) do take into account the azimuthal intensity asymmetries, while they are not originally taken into account in the error bars from the visibility fits. The ratio of azimuthal asymmetry ($\Delta_{\rm img}/I_{\rm img}$) is small in all cases, confirming that the axisymmetric assumption is a good approximation of the disk morphologies. We add the azimuthal asymmetries error bars computed in the image plane to the radial profile uncertainty computed from the visibility fit ($\Delta_{\rm vis}$) as $\Delta I = \sqrt{(\Delta_{\rm vis})^2 + (I_{\rm vis}\Delta_{\rm img}/I_{\rm img})^2}$, where $I_{\rm vis}$ is the intensity radial profile from the visibility fit. These uncertainties are included in the radial profiles of Figure 4. The bottom panels of the same Figure show the flux calibration error bar for all wavelengths. This uncertainty dominates by far the uncertainty in each radial profile.

The radial profiles from the visibility fit reveal higher contrasts between rings and gaps compared to the azimuthal radial profiles computed from the CLEAN images (Figure 1). For example, in the brightness radial profile of LkCa15 in Bands 6 and 7, we clearly identify three main rings from the visibility fit (at 0.″277, 0.″433, 0.″635, as also reported by F. Long et al. 2022). Additionally, there is a tentative faint ring around ∼1.″07, which is also visible in the radial profile of the Band *Q* image, albeit at a radius of ∼0.″99. Note that the width of the rings at 0.″433, 0.″635 in Band 6 looks narrower than those at Band 7, possibly due to dust traps (P. Pinilla et al. 2012a). Additionally,

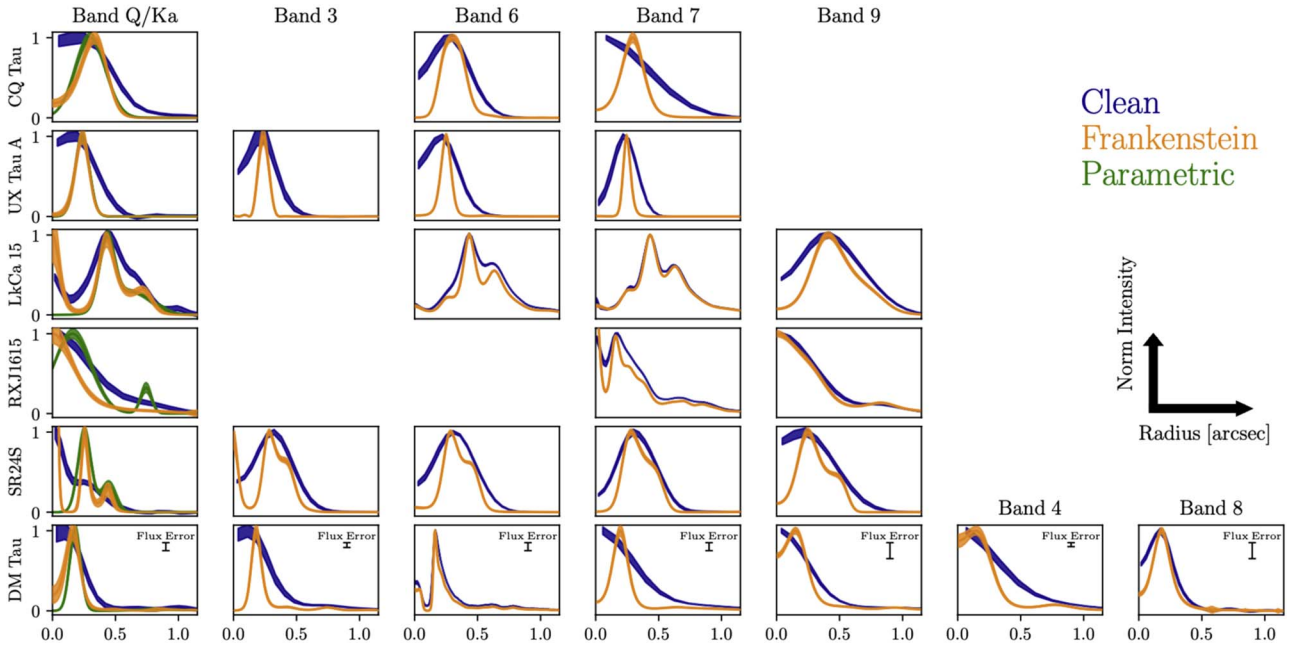

Figure 3. Normalized brightness radial profile for each observation in our sample. The blue lines are the azimuthal average computed from the image plane in Figure 1, the orange lines are the nonparametric radial profile computed with FRANKENSTEIN, and the green lines for the VLA observations are the parametric radial profiles. The vertical error bars in the bottom panels show the uncertainty from the flux calibration at each Band.

the contrast between the rings and gaps is more pronounced in Band 6, likely due to optical depth effects. These characteristics and differences are crucial when constraining the radial profiles of dust properties in Section 4.

The parametric model for all disks was chosen based on the morphology observed at ALMA. For example, in LkCa15, the parametric model is given by two Gaussian functions at a fixed radial position of 0.″433, 0.″635, and a point source at the disk center. We also tested the inclusion of the ring structures at 0.″277 and 0.″99. However, the chi-square value (χ^2) does not exhibit a significant improvement when these rings are added to the model.

The radial profiles in Figure 3 are shown at their intrinsic angular resolution. Starting from Section 4 and beyond, the radial profiles for a specific disk are convolved to the same angular resolution, corresponding to the lowest angular resolution among the multiwavelength observations of each disk.

As mentioned in Section 3.2, the FRANKENSTEIN visibility model is influenced by bin size and hyperparameters for the VLA observations with low SNR. Conversely, the parametric fit provides a robust radial profile. Consequently, the parametric model is selected as the radial profile model for VLA data across all disks. Table 5 in Appendix B.2 provides a summary of the chosen parametric models for each disk and the best-fit parameters.

Figure 8 in Appendix B.1 shows the CLEAN image of the disk models (sampled at the same *uv*-coverage as the observations). The color scale is the same as each panel in Figure 1. The difference between observations and model (Residuals) is shown in Figure 9. Although most of them have low nonaxisymmetric residuals, some exceed $+5\sigma_{\rm rms}$ or fall below $-5\sigma_{\rm rms}$. Various factors may contribute to these residuals, such as the disk potentially being brighter at the inner wall of the ring on the far side due to disk inclination, uncertainties in parameters like disk inclination, PA, disk center, or elevated emission surfaces (S. M. Andrews et al. 2021). Also note that most of the azimuthal asymmetries observed at very long wavelengths (VLA observations) have an SNR <3, making it difficult to distinguish them from thermal noise. The specific disk structures are further discussed in Section 5.

4. Constraints on Dust Properties

The spatially integrated dust continuum emission at millimeter wavelengths has been used to infer dust properties of protoplanetary disks, including mean temperature, optical depths, average maximum grain size, and dust mass. This is typically achieved by fitting a blackbody model to their SED (e.g., A. M. Rilinger et al. 2023).

Owing to the lack of multiwavelength observations at high angular resolution, the spatial modeling of SED has only been spatially modeled in a small fraction of disks (e.g., L. M. Pérez et al. 2012; Y. Liu et al. 2017; C. Carrasco-González et al. 2019; A. Sierra et al. 2021; E. Macías et al. 2021). In this work, we are able to resolve the expected optically thick rings around six transition disks and model the SED as function of radius. Figure 4 shows the brightness temperature for the six transition disks in this work. The radial profiles of each disk are convolved to the same angular resolution (indicated by the horizontal bar in each panel), determined by the lowest angular resolution detailed in the last column of Table 3. The effect of radial beam smearing is discussed in Appendix C.

Note that not all wavelengths were included in our multiwavelength analysis. We opted to exclude observations with low angular resolution (compared with the rest of the multiwavelength data) and avoided convolving most of the observations using a large beam. Additionally, we also decided to neglect the short wavelength observations at Band 9 because they likely primarily capture dust emission from the upper layers of the disk, where smaller grain sizes are expected compared to those traced by longer wavelengths in the

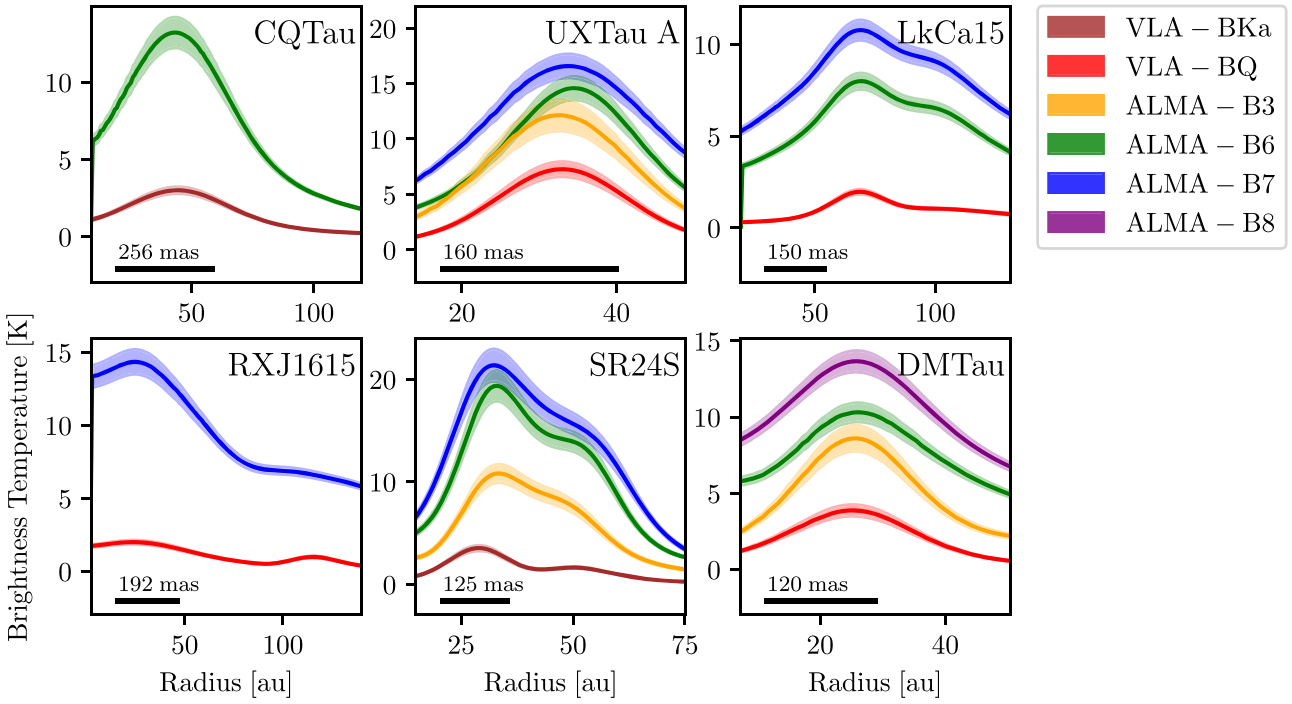

Figure 4. Brightness temperature radial profile for the six transition disks used in the multiwavelength analysis. The common angular resolution for all wavelengths in each disk is shown as a horizontal black line in each panel. The error bar for each profile is computed from errors from the flux calibration, visibility fit, and azimuthal variations.

midplane (e.g., A. Sierra & S. Lizano 2020). The last column in Table 3 summarizes which data sets are used in the multiwavelength analysis.

The SED is fitted at each radius using the emergent intensity of the dust continuum emission at frequency ν in A. Sierra & S. Lizano (2020), which is given by

$$I_\nu = B_\nu(T_d)[1 - \exp(-\tau_\nu/\mu) + \omega_\nu F(\tau_\nu, \omega_\nu)], \quad (3)$$

where $B_\nu(T_d)$ is the Planck function evaluated at the dust temperature T_d, τ_ν is the optical depth, μ is the cosine of the disk inclination, ω_ν is the dust albedo, and $F(\tau_\nu, \omega_\nu)$ is the contribution of scattering to the emergent intensity, given by

$$F(\tau_\nu, \omega_\nu) = \frac{1}{\exp(-\sqrt{3}\,\epsilon_\nu\tau_\nu)(\epsilon_\nu - 1) - (\epsilon_\nu + 1)} \times \left[\frac{1 - \exp(-(\sqrt{3}\,\epsilon_\nu + 1/\mu)\tau_\nu)}{\sqrt{3}\,\epsilon_\nu\mu + 1} + \frac{\exp(-\tau_\nu/\mu) - \exp(-\sqrt{3}\,\epsilon_\nu\tau_\nu)}{\sqrt{3}\,\epsilon_\nu\mu - 1}\right], \quad (4)$$

where $\epsilon_\nu = \sqrt{1 - \omega_\nu}$. The main effect of scattering (Equation (4)) is decreasing the emergent intensity in the optically thick regime, making it possible to explain spectral indices below 2, as discussed in previous works (e.g., H. B. Liu 2019; Z. Zhu et al. 2019; A. Sierra & S. Lizano 2020).

The albedo and absorption dust opacity coefficient κ_ν are taken from T. Birnstiel et al. (2018), and the dust grains are assumed to follow a particle size distribution (number of grain sizes per size bin) given by $n(a)da \propto a^{-p}da$, where the minimum grain size is fixed to 0.05 μm, and the maximum grain size $a_{\rm max}$ is a free parameter. The slope of the particle size distribution p is fixed to 3.0. The expected value from simulations is between 2.5 and 3.5, when the maximum grain size is regulated by drift and fragmentation, respectively (T. Birnstiel et al. 2012b). However, we tested p values within this range, and the qualitative conclusions are not sensitive to this particular choice.

Equation (3) can be evaluated given the dust temperature $T_{\rm d}$, maximum grain size $a_{\rm max}$ (which controls ω_ν and κ_ν), and dust surface density $\Sigma_{\rm d}$ (which controls the total optical depth: $\tau_\nu = \kappa_\nu\Sigma_{\rm d}/(1 - \omega_\nu)$). We use an MCMC method (implemented in the PYTHON library EMCEE, D. Foreman-Mackey et al. 2013) using 24 walkers and 10,000 steps to explore the space parameter of $a_{\rm max}$, $\Sigma_{\rm d}$, and $T_{\rm d}$ at each radius. The chi-squared in the posterior distribution is defined as

$$\chi^2 = \sum_n \left(\frac{I_{\nu_n} - I_{\nu_n}^{\rm model}}{\Delta I_{\nu_n}}\right)^2, \quad (5)$$

$I_{\nu_n}^{\rm model}$ is the model intensity evaluated from Equation (3), and ΔI_{ν_n} is the uncertainty of the nth intensity. The absolute flux uncertainty is taken into account in δI_{ν_n} at each band according to the ALMA proposer's guide: 5% in Band 3 and 4, 10% in Band 6 and 7, and 20% in Bands 8 and 9.

The prior is given by $p(a_{\rm max}) \times p(\Sigma_{\rm d}) \times p(T_{\rm d})$, where $p(a_{\rm max})$, $p(\Sigma_{\rm d})$ are the maximum grain size and dust surface density priors, given by a log-uniform distribution within the explored parameter space, and the temperature prior is defined as

$$p(T_{\rm d}) = \exp\left[-\frac{1}{2}\left(\frac{T_{\rm prior} - T_{\rm d}}{\sigma_{T_{\rm prior}}}\right)^2\right], \quad (6)$$

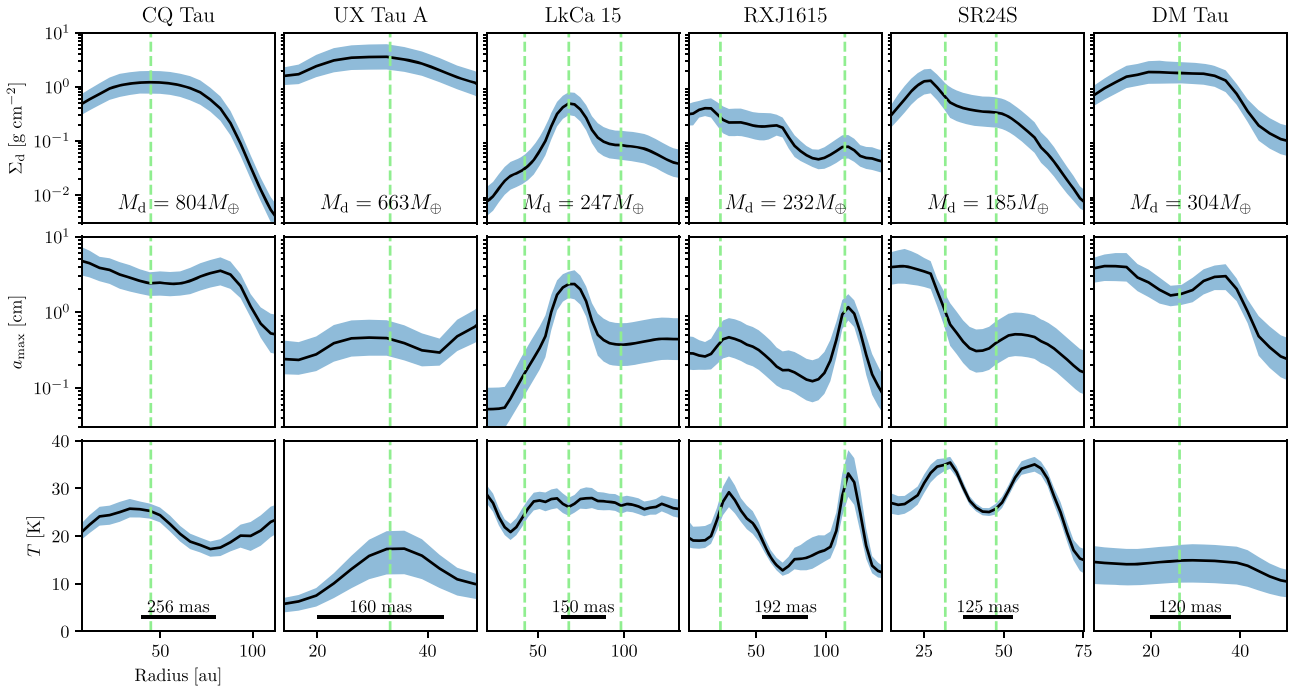

Figure 5. Dust surface density (top panels), maximum grain size (middle panels), and dust temperature (bottom panels) constraints from the SED fit. The vertical dashed lines mark the position of bright rings inferred at higher angular resolution. The inferred dust mass and angular resolution of each disk are shown in the bottom of the top and bottom panels, respectively.

i.e., the probability of a model with a temperature T_d decreases if it deviates from T_{prior}. The latter is computed from the temperature of an passively irradiated disk $T_{prior} = (0.02L_*/8\pi\sigma_B r^2)^{1/4}$. We use a wide temperature width $\sigma_{T_{prior}} = 50$ K to ensure that this prior does not dominate the posterior probability distribution.

The inclusion of this prior decreases the degeneracy between the free parameters, especially when the number of wavelengths used to fit the SED is less than or equal to the number of free parameters.

The explored parameter space is log-spaced between 300 μm $\leqslant a_{max} \leqslant$ 30 cm, 10^{-6} g cm$^{-2} \leqslant \Sigma_d \leqslant 10$ g cm^{-2}, and 3 K $\leqslant T_d \leqslant$ 300 K. The smallest value for the maximum grain size is chosen to avoid degeneracy between a small-grain solution ($a_{max} < 300$ μm) and large grains ($a_{max} \geqslant 300$ μm). As shown in Figure 4 of T. Birnstiel et al. (2018), the spectral index around 300 μm is degenerated for large or small grain sizes. However, we also did some tests including small maximum grain sizes $a_{max} = 10$ μm, but found that the walkers tend to the large maximum grain size regime after sufficient steps. The inclusion of small maximum grain sizes ($a_{max} < 300$ μm) only delays the walkers from reaching the space parameter with the maximum posterior probability ($a_{max} \geqslant 300$ μm.)

The best fit of each parameter is shown in Figure 5 for the six transition disks in this work. The vertical lines mark the position of the rings inferred from the visibility fit (Section 3). The error bars are computed from the percentiles 32 and 68 respectively. The dust mass is shown in the bottom of each top panel, while the angular resolution of each disk is shown in the bottom panels.

Figure 6 shows the optical depth constraints resulting from the dust properties in Figure 5 at different wavelengths.

5. Discussion

The results from the disk substructures computed from the visibility fit for each observation (Figures 2 and 3), and the dust property constraints from the multiwavelength fit (Section 4), give clues about the physical origin of the large cavities observed in the six transition disks in this work. However, before discussing the results from each individual disk (Sections 5.2–5.3), we summarize the various caveats associated with our modeling below.

5.1. Model Limitations

The exact dust properties inferred from the multiwavelength analysis depend on the physical assumptions described in the previous section (e.g., particle size distribution slope, spherical and compact dust grains). However, general properties, such as the peak position of the dust surface density or maximum grain size, are unchanged under these physical assumptions.

The maximum grain size estimations in this work are similar to previous analysis where the dust continuum SED has been modeled, and where millimeter and centimeter grain sizes have been inferred (e.g., L. M. Pérez et al. 2012; C. Carrasco-González et al. 2019; T. Ueda et al. 2020). However, it is important to remark that smaller grain sizes (hundreds of microns or smaller grain sizes) have been inferred from polarized observations (e.g., A. Kataoka et al. 2016b; C. L. H. Hull et al. 2018; T. Mori et al. 2019). Our results are biased by the spectral index analysis. Alleviating the tension between the grain size estimations from polarization and spectral index is beyond the scope of this paper. An exception to the SED modeling has been found in the disk around DMTau (H. B. Liu et al. 2024), where the dust emission from localized substructures is consistent with $a_{max} \gtrsim 300$ μm, but the rest of the disk is consistent with small grains ($\lesssim$50 μm).

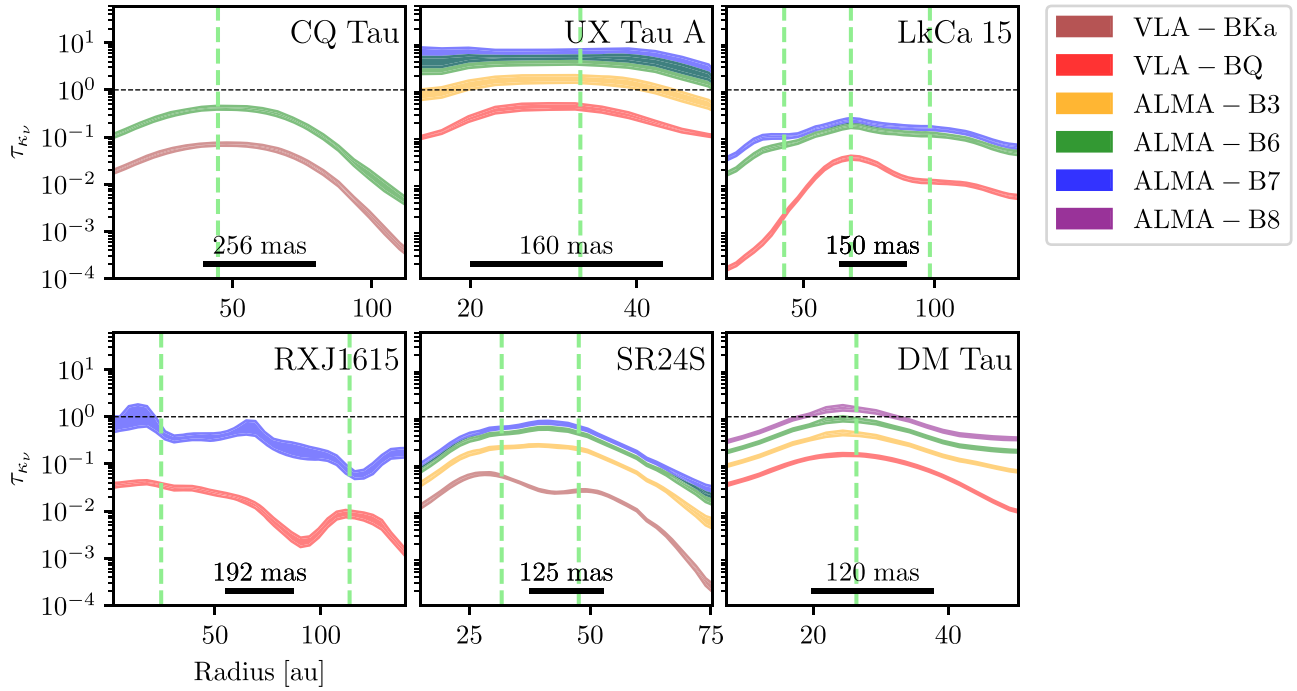

Figure 6. Optical depth radial profiles computed from the SED fit at different wavelengths (see color code). The vertical dashed lines mark the position of bright rings inferred at higher angular resolution. The horizontal bar of each panel shows the angular resolution for each disk.

On the other hand, angular resolution limitations could impact the inferred dust properties profiles. In particular, the disk cavities could potentially be contaminated by emission from optically thick rings. In such cases, the cavities would present faint emission with low spectral indices, which can be interpreted as optically thin emission with large grain sizes. Given the angular resolution of the data, it is not possible to rule out the possibility of smearing effects within the cavities, especially in those disks where large grain sizes are inferred in this region. A full discussion of the radial smearing effects is presented in Appendix C. We also emphasize that our method for inferring the intrinsic angular resolution of a FRANKENSTEIN fit does not assess the ability of such a fit to resolve two independent structures (e.g., two rings). Rather, the intrinsic angular resolution corresponds to the "point-spread function" (PSF) of a FRANKENSTEIN fit done to an infinitely narrow ring. We tested different models with smaller separations between the two rings, but there is no clear limit at which the visibility fit is unable to separate them. The only limit is given by the sampling of the radial profile, which is not a physical measurement of the angular resolution, but is determined by the Nyquist sampling theorem (A. R. Thompson et al. 2017), which should always be satisfied. See more details in Appendix A.

Additionally, we assume that the disks are axisymmetric and compute their azimuthally averaged properties. However, some degree of asymmetry has been observed in some of them (see references in the discussion of each particular disk). In a few cases, these asymmetries are consistent with thermal noise (especially at long wavelengths).

Although we only study the multiwavelength emission in a radial extend where the azimuthal asymmetries are low or negligible (See Section B.1), the dust properties' constraints in this work only pretend to explain the azimuthally averaged dust properties of each analyzed disk, and a bidimensional analysis of the disks is beyond the scope of this work. In some cases, such as DMTau, the axisymmetric structure observed at ALMA Bands, and the azimuthal asymmetries observed at Band *Q* may be explained by optical depth effects (see discussion in H. B. Liu et al. 2024). In such cases, the constraints on the dust properties are mainly dominated by the morphology observed at ALMA wavelengths.

5.2. Disks with Dust Traps as a Possible Origin of the Cavity

Disks with dust surface density and grain size maxima at ring positions are consistent with dust trap models (P. Pinilla et al. 2012b). The dust trap can be induced by a companion (a planet or a close binary) or a dead zone. However, if a deep gas cavity is also observed, it rules out the possibility of a dust trap created by a dead zone (N. van der Marel et al. 2016), and supports the idea of a companion origin. In the following, we discuss the results obtained from disks where both a dust trap (identified in this work) and gas cavities (from the literature) have been inferred. These findings may suggest that the origin of these large cavities is a companion.

UXTau A. Dust continuum observations of the disk around UXTau A have been previously reported by P. Pinilla et al. (2018) and L. Francis & N. van der Marel (2020). From the visibility modeling in this work (Figure 3), we confirm the ring-shaped structure, with a peak at $0\farcs236$ (33.0 au). Additionally, the disk emission exhibits azimuthal asymmetries at Bands 6 and 7 (Figure 9), with higher intensities observed toward the east. The Band 3 image appears nonaxisymmetric, but these asymmetries are created by the visibility coverage and the elongated beam, as shown by the perfect axisymmetric disk model sampled at the same visibilities in Figure 8. This is demonstrated in the model image of a perfectly axisymmetric disk. Similarly, Band *Q* exhibits azimuthal structures along the major axis of the beam. The residuals of the enhanced emission at the south of the disk in Band *Q* have an SNR < 5, as shown in Figure 9.

The dust properties' constraints (Figure 5) show a peak in the dust surface density, maximum grain size, and dust temperature aligning with the location of the main ring, exhibiting characteristics consistent with dust trap signatures, which can be triggered by a companion or a dead zone.

No planet candidates have been found in UXTau A using Hα observations (A. Zurlo et al. 2020). The sensitivity of the Hα observations is consistent with a upper limit to the mass of the planet of 9 Jupiter mass at $\sim$22 au. The ^{12}CO (J : 3–2) observations in L. Wölfer et al. (2023) reveal a gas cavity and a ring structure in the gas that peaks near the dust ring.

LkCa15. Dust continuum observations of the disk around LkCa15 at high resolution have been studied by A. Isella et al. (2014), S. Facchini et al. (2020), and F. Long et al. (2022), where three rings at at 0.″277 (43.5 au), 0.″433 (68.1 au), 0.″636 (100 au) have been inferred from the radial profiles in the image plane and from visibility modeling. We note a fourth faint outer ring at 1.″070 (168.2 au) from both the image plane and visibility modeling at ALMA wavelengths. This faint ring can also be inferred from the radial profile in the image plane at Band Q, but at a slightly smaller radius of 0.″990 (155.6 au).

The visibility modeling residuals at Band 6 and 7 in Figure 9 matches with those in F. Long et al. (2022). At Band Q, there are no residuals with SNR >5. And at Band 9, there are positive/negative residuals in the far/near-side part of the disk, possibly due to an elevated emission surface at Band 9 (S. M. Andrews et al. 2021), where the emission of small grains is traced.

The results from the SED fit in Figure 5 for LkCa15 show three local maxima for the dust surface density, aligning precisely with the radial positions of the three prominent rings observed in the dust continuum emission. The maximum grain size only has a clear peak around the main ring at 0.″433 (68.1 au) at this resolution. These characteristics are indicative of dust trapping in the main ring, impeding the inward flow of dust grains and forming a large cavity.

No clear planetary signatures have been directly detected within the LkCa15 cavity, although planet candidates have been suggested (e.g., A. L. Kraus & M. J. Ireland 2012). Comparing SPHERE/ALMA observations and the size of the observed gaps, G. Lodato et al. (2019) and R. Asensio-Torres et al. (2021) estimated that the upper limit of the mass of a planet companion within the cavity is $\lesssim$1 Jupiter mass. On other side, the Lagrangian points identified by F. Long et al. (2022) suggest the possible existence of a Neptune-mass planet positioned at a projected distance of 0.″27 (42.4 au).

Finally, evidence of a gas cavity has been found in the molecular emission of ^{12}CO ($J=2$–1), ^{13}CO ($J=2$–1), and C^{18}O ($J=2$–1) (L. Wölfer et al. 2023), suggesting that the origin of the cavity is a companion.

RXJ1615. Millimeter dust continuum observations of the disk around RXJ1615 have been previously reported by N. van der Marel et al. (2015) and L. Wölfer et al. (2023). The visibility modeling of the disk is shown in Figures 2–3. At Band 9, the visibility modeling is sensitive to a ring at 0.″82 (127.6 au), while a discernible dust cavity is absent, likely due to the limited angular resolution. The outer dust ring had previously been identified by S. M. Andrews et al. (2011) and N. van der Marel et al. (2015).

At Band 7, the radial profile shows a complex structure. Notably, it exhibits emission from various sources: a distinct compact inner disk, an asymmetric ring with a prominent peak at 0.″158 (24.6 au), along with additional local peaks at approximately 0.″251 (39.0 au) and 0.″368 (57.3 au). Moreover, two further asymmetric peaks emerge at around 0.″685 (106.6 au) and 0.″839 (130.5 au), distinguishable in both the visibility fit and the image plane. Overall, the observations reveal the presence of up to five discernible rings and an inner disk. In Band Q, the FRANKENSTEIN visibility fit fails to identify disk substructures, unlike the parametric fit, which successfully does. This is the only disk where the position of the outer ring is not fixed, but it is a free parameter (Table 5). The best-fit radial position for the outer ring is $0.73^{+0.05}_{-0.08}$, falling between the locations of the two outer rings observed in Band 7.

The dust surface density and maximum grain size (Figure 5) have clear local maxima at the outer ring, aligning with dust trap signatures. However, there is no clear evidence of a pressure trap in the inner ring (although it is suggested), due to the low angular resolution, which is not able to resolve the inner ring after convolution (beam size of 0.″192 and a ring at 0.″158; see Figure 4).

The findings in the outer ring align with dust trap signatures. On the other hand, a gas density drop has been detected within the disk cavity, as reported by N. van der Marel et al. (2015), suggesting that the origin of the cavity is a companion. The mass of the companion candidate has been estimated as 4.5 Jupiter masses using SPHERE observations (R. Asensio-Torres et al. 2021).

5.3. Disks with Possible Evidence of Enhanced Grain Growth and a Pressure Trap as the Origin of the Cavity

In some of our transition disk sample, the inferred maximum grain size radial profile ($a_{\max}(r)$) monotonically decreases with radius, rather than showing a distinct drop within the cavity. Additionally, the distribution of $a_{\max}(r)$ appears relatively flat around the ring region, possibly indicating the presence of a dust trap. On the other hand, the dust surface density radial profile shows a drop of mass within the cavity. The millimeter emission cavity in these cases is reproduced by a combination of very low densities and large dust grains with low opacity. As mentioned in Section 1, these characteristics are expected for cavities created by grain growth and a pressure bump. Grain growth alone is insufficient to reproduce the low brightness within the cavity, and a pressure bump (created by a companion or a dead zone) is crucial for efficiently reducing the mass within the cavity (T. Birnstiel et al. 2012a).

The absence of a gas gap within some of these disks further would suggest that the origin of the large cavity is not the same as in the rest of the disks. However, as mentioned at the beginning of this section, radial smearing of optically thick emission onto the cavity regions could affect the inferred dust properties. In particular, radial smearing could mimic large dust grain sizes within the cavity, as discussed in Appendix C. In the following, we discuss the results obtained from disks where a possible origin of the dust cavity may be attributed to low dust surface density triggered by a pressure bump in the ring, coupled with enhanced grain growth within the cavity, and where deep gas cavities have not been observed.

CQTau. The disk morphology of the dust continuum emission around CQTau has been previously reported at high angular resolution by P. Pinilla et al. (2018) and M. G. Ubeira Gabellini et al. (2019). From the visibility modeling in this work (Figure 3), we confirm the ring shape structure at Band 7,

6, and *Ka*, with a peak at 0.″3 (44.8 au). The ring structure is also inferred from the image plane for Bands 6 and *Ka*. However, for Band 7, the angular resolution in the image plane smears the ring emission within the cavity, making it discernible only through the visibility fit.

According to M. G. Ubeira Gabellini et al. (2019), the disk emission displays azimuthal asymmetries in both the continuum and CO isotopologue lines. These nonaxisymmetric structures are shown in Figure 9. At Band 6, the disk emission appears brighter in the east and southwest regions compared to the average azimuthal values. A noticeable azimuthal asymmetry is also observed in the southwest of the disk at Band *Ka* (Figure 9). However, this particular asymmetry has an SNR <5.

The dust properties' radial profiles for CQ Tau show a dust surface density with a peak at the ring position. The maximum grain size monotonically decreases with radius, suggesting no strong evidence of a dust trap (at this angular resolution). However, a gas cavity has been inferred from the CO isotopologue emission in M. G. Ubeira Gabellini et al. (2019). Their work shows that the gas cavity is consistent with a planet of 6–9 Jupiter masses located 20 au from the central star. Given the gas and dust observations, it is not clear what mechanism is able to explain the cavity observed in dust continuum emission for CQ Tau.

SR24S. High angular resolution of the disk around SR24S at millimeter wavelengths has been previously reported by P. Pinilla et al. (2017), L. A. Cieza et al. (2021), and L. Francis & N. van der Marel (2020). The visibility modeling for SR24S (Figures 2–3) shows an asymmetric ring structure at all wavelengths, similar to two adjacent ring structures, with peaks at ∼0.″254 (29.0 au), 0.″441 (50.3 au). The asymmetric ring has been already reported in previous works (e.g., L. A. Cieza et al. 2021). The FRANKENSTEIN and parametric fit at Band *Ka* are able to resolve the two rings, at the same radial location observed in the ALMA data.

The dust properties' constraints for SR24S show a dust surface density increasing toward the two rings; however, the maximum grain size decreases with radius, and it only has a flat distribution around the ring at 0.″254 (29.0 au). Large dust grain sizes are inferred within the cavity, suggesting that enhanced grain growth and a pressure bump are responsible of the deficit of millimeter emission in this region.

SR24S is the only disk among the transition disks studied by N. van der Marel et al. (2015) where a drop of at least 1 or 2 orders of magnitude in the gas surface density within the disk cavity is not inferred. P. Pinilla et al. (2020) confirmed that the optically thin molecular emissions of ^{13}CO and C^{18}O peak at the center of the disk cavity, indicating no gas deficit within the inner cavity of the disk, unlike many transition disks. As pointed out by P. Pinilla et al. (2020), a large cavity created by photoevaporation is unlikely due to the high accretion rate, the large dust cavity, and the gas emission within this region.

DMTau. Millimeter dust continuum observations of the disk around DMTau at high resolution have been previously studied by many authors at several wavelengths, including S. M. Andrews et al. (2011), D. Semenov et al. (2018), J. Hashimoto et al. (2021), and H. B. Liu et al. (2024).

The observations presented by J. Hashimoto et al. (2021) at high angular resolution reveal an inner ring (<0.″1, 14.4 au), a main ring with a peak at ∼0.″16 (23.0 au), and two extended faint ring structures, as shown in the radial profile from the visibility fit at Band 6 in Figure 3. The main ring at this wavelength only presents weak azimuthal asymmetries, likely due optical depth effects. These asymmetries are better observed at optically thinner wavelengths using JVLA observations at Band *Q* (H. B. Liu et al. 2024), where a visibility analysis shows that the Band *Q* intensity is azimuthally asymmetric on the spatial scale of ∼20 au or less. The spatial resolution in this work (∼18 au) only marginally resolves those spatial scales.

The primary ring within the disk is consistently identified across all wavelengths in the visibility fit (ranging from Band 9 to Band *Q*). Faint outer structures are evident across all wavelengths, but their radial positions do not align with those observed at Band 6. These faint structures disappear when the radial profiles are convolved at the same angular resolution (Figure 4).

The results from the SED fit for DMTau in this work (Figure 5) show a dust surface density increasing toward the position of the main ring. The maximum grain size decreases with radius, and it has a flat distribution close to the disk ring. Evidence of efficient grain growth in the innermost region of DMTau has been also found by J. Hashimoto et al. (2021). They found that the SED can be reproduced using a population of large dust grains (millimeter grains) that are less depleted than small dust grains (submicron size), consistent with efficient grain growth in the inner region of the disk, consistent with our grain size estimations within the cavity. However, the multiwavelength analysis in H. B. Liu et al. (2024) recently showed that the integrated SED from 8 to 700 GHz can be explained by two grain size components: one population of $a_{\max} \gtrsim 300$ μm sizes for the emission of small solid angles (as the knot observed in Band *Q*), and a second population of $a_{\max} < 50$ μm for larger solid angles (similar to the spatial scale emission from ALMA wavelengths). These analyses and their apparent disagreement show why higher angular resolution observations where the emission from compact and extended sources can be resolved at several wavelengths.

No evidence of a gas gap has been found within the dust cavity (T. Kudo et al. 2018; J. Hashimoto et al. 2021; N. van der Marel et al. 2021), although the ^{12}CO observations used in these works may not be able to resolve the gap, and the emission could be optically thick. L. Wölfer et al. (2023) studied the spatial distribution of optically thinner molecular transitions in DMTau, including ^{13}CO and C^{18}O, but no evidence of a deep gas cavity or spirals'/arcs' structure was found, although the angular resolution could also be insufficient. Therefore, the presence of a possible gas gap inside the dust cavity is still unknown.

As pointed out by T. Kudo et al. (2018), the origin of the dust cavity remains unclear. The high accretion rate disfavors photoevaporation, while the absence of a gas gap (L. Wölfer et al. 2023) disfavors a companion. In any case, a pressure bump at the ring location is needed to explain the deficit of dust mass within the cavity.

6. Does the Origin of a Large Cavity Depend on the Disk Mass?

The constraints on dust properties shown in Figure 5 offer insights into the origin of the observed large cavities. The results suggest that, in UXTau A, LkCa15, and RXJ1615, the origin of the large cavities are dust traps created by a companion (a planet or a close binary). Conversely, in CQTau,

Table 4
Compatibility of the Different Large Cavity Origins and the Observational Signatures Found in Each Disk

	This Work						Literature	
	CQTau	UXTau A	LkCa15	RXJ1615	SR24S	DMTau	GMAur	Sz91
$M_*[M_\odot]$	1.63	1.4	1.32	1.1	0.87	0.39	1.1	0.54
$M_{\rm dust}[M_\oplus]$	804	663	247	232	185	305	245	31.3
Dust trap companion	→	✓	✓	✓	→	→	→	→
Dust trap dead zone	→	✓	✓	✓	→	→	→	→
Grain growth	✓[a]	✗	✗	✗	✓[a]	✓[a]	✓[a]	✓[a]
Photoevaporation	✗	✗	✗	✗	✗	✗	✗	✗
Gas cavity[b]	✓	✓	✓	✓	✗	✗[d]	✓	✓
Kinematic spirals/arms[c])	✓	✓	→	✓	···	✗	✗	→

Notes. ✓: Compatible. ✗: Not compatible. →: Tentative.
[a] Possibly affected by radial smearing of low angular resolution observations.
[b] Gas constraints from literature (references in Sections 5.2–5.3).
[c] From kinematic signatures in L. Wölfer et al. (2023).
[d] Low angular resolution observations. Stellar mass references: GMAur (E. Macías et al. 2018), Sz91 (L. Francis & N. van der Marel 2020), and those in Table 1.

SR24S, and DMTau, a possible origin of the large cavities is a combination of monotonically increasing maximum grain size toward the disk center (which results in low emission at millimeter wavelengths), and a deficit of dust mass created by a pressure bump in the ring (T. Birnstiel et al. 2012a). In the latter scenario, the pressure bump can be generated, for example, by a dead zone or a companion.

It is important to note that resolution effects may play a significant role in inferring the increasing maximum grain size toward the disk center, possibly due to the presence of inner disks, as shown in the brightness radial profile of SR24S at Band 3 or DMTau at Band 6 (Figure 3). Although the inner disks vanish when convolved to a lower angular resolution (Figure 4), their emission could spread to outer radii within the cavity (see discussion in Appendix C).

Table 4 summarizes various physical mechanisms consistent with the observational signatures presented in this work. Additionally, it includes constraints on gas cavities, and the detection of spirals/arms in CO maps, which have been interpreted as potential evidence of embedded companions (L. Wölfer et al. 2023). It is also important to remark that no evidence of inner brown dwarf companions with a mass >20 $M_{\rm Jup}$ has been found in UXTau A, LkCa15, RXJ1615, and SR24S, while it is only tentative for DMTau (A. L. Kraus et al. 2011).

The reported dust masses in Table 4 are estimated by integrating the dust surface density profiles in Figure 5. The final columns present similar observational signatures observed in two other transition disks (GMAur, Sz91), where multi-wavelength modeling has also been used to infer dust properties' radial profiles.

The dust properties in the disks around GMAur (A. Sierra et al. 2021) and Sz91 (K. Maucó et al. 2021) show dust surface density maxima at the position of the rings, and a maximum grain size decreasing with radius, consistent with a large cavity created by a pressure bump and enhanced grain growth. However, radial smearing effects within the cavity cannot be ruled out given the spatial resolution of the observations. However, unlike SR24S and DMTau, gas cavities have been observed in GMAur and Sz91, and tentative kinematic spirals/arms in Sz91.

In our sample, the disk dust mass generally tends to increase with the stellar mass, as already reported by P. Pinilla et al. (2020) in a large sample of disks. Note that the origin of the large cavities with the lowest stellar/dust mass in our sample is tentatively attributed a pressure bump and enhanced grain growth. Conversely, for higher stellar/dust masses, except possibly CQTau, the large cavities are consistent with dust traps formed by a companion. It is important to remark that the long wavelength data in this work (from DisksEVLA project, ID: AC982) are biased toward massive disks. Thus, a larger sample of transition disks covering lower disk masses is needed to confirm or rule out our suggestive findings, in addition to higher angular resolution, which can help rule out radial smearing effects.

It is known that disk mass can play a role in shaping the formation, evolution, and characteristics of protoplanetary disks (e.g., Á. Ribas et al. 2015; J. Drkażkowska et al. 2023, and references therein). In transition disks, the origin of the cavities could be mass dependent, as suggested by the results in this work. Further observational modeling, high angular resolution data, and simulations are necessary to delve deeper into exploring this possibility.

7. Conclusions

We analyzed millimeter dust continuum observations of transition disks surrounding CQTau, UXTau A, LkCa15, RXJ1615, SR24S, and DMTau. A total of 26 observations were used, covering wavelengths from ALMA Band 9 (435 μm) to VLA Band *Ka* (8.8 mm). These observations were used to fit the radial brightness profiles at subbeam resolution, enabling a study of the radial distribution of solids.

The constraints on the dust surface density, dust temperature, and maximum grain size radial profiles inferred from modeling the SED offer valuable insights regarding the physical origin of the observed large cavities in each disk. Our main conclusions about the disk morphology and origin of the large cavities in each disk are summarized as follows.

1. The radial brightness profiles observed in the disks around CQTau and UXTau A reveal a Gaussian-like ring at all wavelengths, and no emission from an inner disk. Additionally, the point source at the longest VLA wavelengths is consistent with a notably low flux (upper limit of $\lesssim$7 μJy) in both disks.

2. Across multiple wavelengths, the brightness radial profiles observed in the disks around RXJ1615, LkCa15, SR24S, and DMTau display a multiring structure. Notably, RXJ1615 exhibits the highest number of discernible substructures, particularly evident at Band 7 where the high angular resolution enables the identification of up to five local maxima and an inner disk. In LkCa15 and SR24S, the number of rings or local maxima is four and two, respectively.

   In the case of DMTau, the primary ring observed at the Band 6 wavelength displays asymmetry. Additionally, this profile shows two faint rings in the outer disk, which are poorly constrained across other wavelengths. The disks associated with RXJ1615, LkCa15, SR24S, and DMTau have an inner disk, which can be observed at the highest angular resolution observations.
3. The radial profiles of the dust surface density and maximum grain size in the disks around UXTau A, LkCa15, and RXJ1615 have peak values at the position of the main ring of each disk. These properties align with dust trap models, which may be formed by either a companion or a dead zone. Gas observations of these disks have unveiled gas cavities and kinematic spirals/arms, indicating that the formation of the dust trap and the large cavities in these disks could be attributed to a companion carving a deep gap.
4. In CQTau, SR24S, and DMTau, the dust surface density peaks at the ring positions, whereas the maximum grain size decreases with radius, displaying a plateau around the rings. Although the inferred large grain sizes within the cavity can be affected by radial smearing, these large grain sizes are able to reproduce the multiwavelength observations. These findings suggest the possibility that large grains (with low opacity at millimeter wavelengths) are present in the cavity (unlike the other disks in this work), while the low dust surface densities constrained in the cavities might be triggered by a pressure bump in the ring (either by a companion or dead zone). No gas cavities and kinematic spirals/arms in molecular gas observations have been observed in SR24S and DMTau, suggesting that the origin of their cavities may differ from the rest of the disks in this work. However, the low angular resolution of existing dust continuum and molecular gas observations are not sufficient to favor a particular mechanism.
5. The dust properties' constraints in the transition disks in our sample may exhibit different characteristics, suggesting potentially different origins for the large cavities. In most of the massive disks (UXTau A, LkCa15, RXJ1615), the cavity formation can be attributed to a dust trap created by a companion. In contrast, for the less massive disks (SR24S, DMTau), the cavities may result from a deficit of dust mass created by a pressure bump and enhanced grain growth, leading to a reduction in the emergent intensity within the cavity. However, similar constraints are found in the massive disk around CQ Tau. Given the low angular resolution and possible radial smearing, the possibility of small grain sizes within the cavity (as those inferred from polarized observations) consistent with pressure traps cannot be ruled out for CQTau, SR24S, and DMTau.

Acknowledgments

We are very thankful for the thoughtful suggestions of the anonymous referee that helped to improve our manuscript significantly. A.S. acknowledges support from FONDECYT de Postdoctorado 2022 No. 3220495. L.P. acknowledges support from ANID FONDECYT Regular No. 1221442. A.S, L.P., and M.B. acknowledge support from ANID BASAL project FB210003 and Programa de Cooperación Cientifica ECOS-ANID ECOS200049. We thank Nicolas Kurtovic for his help on the calculation of disk offsets and geometry constraints. We thank Elena Viscardi and Enrique Macias for their discussion about the effects of beam smearing and its impact on inferring dust properties. This project has received funding from the European Research Council (ERC) under the European Union's Horizon 2020 research and innovation program (PROTOPLANETS, grant agreement No. 101002188). T.H. acknowledges support from the European Research Council under the Horizon 2020 Framework Program via the ERC Advanced Grant Origins 83 24 28.

This paper makes use of the following ALMA data: ADS/JAO.ALMA No. 2011.0.00320.S, ADS/JAO.ALMA No. 2011.0.00742.S, ADS/JAO.ALMA No. 2012.1.00870.S, ADS/JAO.ALMA No. 2013.1.00091.S, ADS/JAO.ALMA No. 2013.1.00157.S, ADS/JAO.ALMA No. 2013.1.00498.S, ADS/JAO.ALMA No. 2015.1.00296.S, ADS/JAO.ALMA No. 2015.1.00888.S, ADS/JAO.ALMA No. 2015.1.01137.S, ADS/JAO.ALMA No. 2016.1.00565.S, ADS/JAO.ALMA No. 2016.1.01042.S, ADS/JAO.ALMA No. 2018.1.00350.S, ADS/JAO.ALMA No. 2018.1.01255.S, ADS/JAO.ALMA No. 2018.1.01755.S.

ALMA is a partnership of ESO (representing its member states), NSF (USA), and NINS (Japan), together with NRC (Canada), MOST and ASIAA (Taiwan), and KASI (Republic of Korea), in cooperation with the Republic of Chile. The Joint ALMA Observatory is operated by ESO, AUI/NRAO, and NAOJ. The National Radio Astronomy Observatory is a facility of the National Science Foundation operated under cooperative agreement by Associated Universities, Inc.

We acknowledge the use of data from the Very Large Array (VLA) AC982, 12B-196, 13B-381, operated by the National Radio Astronomy Observatory (NRAO). The National Radio Astronomy Observatory is a facility of the National Science Foundation operated under cooperative agreement by Associated Universities, Inc.

Software: Astropy (Astropy Collaboration et al. 2013, 2018), CASA (J. P. McMullin et al. 2007), Emcee (D. Foreman-Mackey et al. 2013), Frankenstein (J. Jennings et al. 2020), Matplotlib (J. D. Hunter 2007), Numpy (C. R. Harris et al. 2020).

Appendix A
Angular Resolution from Visibility Modeling

In Section 4, we fit the SED of the disks as a function of radius. This requires comparing the multiwavelength radial profiles from the visibility modeling at the same angular resolution. The *uv*-coverage of the observations in this work varies significantly. For instance, most of the Band 9 data were collected during ALMA Cycle 0 (in 2012), while some Band 3 or 6 data sets were observed after 2020, where the antenna configuration is more extended. Therefore, we anticipate differences in the intrinsic angular resolution of the visibility

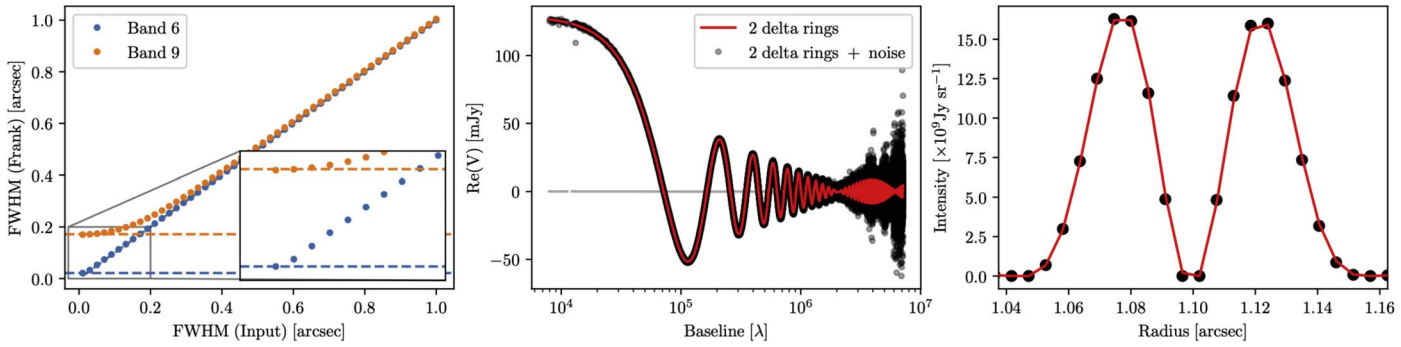

Figure 7. Left: Inferred FWHM of a Gaussian disk as a function of the input FWHM model. The horizontal dashed line is the minimum recoverable spatial scale for a delta ring, which depends on the *uv*-coverage of each observation, such as the Band 6 (blue) and Band 9 (orange) observations of LkCa15. Middle: Real part of the visibilities as a function of baseline for two delta rings separated by 0.″05. The red and black dots represent a model without and with thermal noise, respectively. Right: intensity radial profile obtained from FRANKENSTEIN for the two delta rings without (red) and with thermal noise (black).

fits. As fully discussed in Section 3 in J. Jennings et al. (2020), the visibility fits with FRANKENSTEIN can attain subbeam resolution. To address the angular resolution problem, we test two different methodologies: delta ring, and Gaussian disk, which are described below.

A.1. Delta Ring

We generate synthetic visibility observations of an infinitely narrow ring (a delta function) centered at a radius of $r_0 = R_{\rm max}/2$ (where $R_{\rm max}$ denotes the maximum disk radius from the visibility fit[14]). The center r_0 was chosen to avoid boundary effects. However, negligible differences are found when using a different r_0. The synthetic visibilities of the delta ring $\delta(r - r_0)$ are computed by its Hankel transform $\mathcal{H}$ as

$$\mathcal{H}\left[\frac{A_0}{2\pi r_0}\delta(r - r_0)\right] = A_0 J_0(2\pi r_0 q), \quad \text{(A1)}$$

where A_0 is a constant that represents the total flux, and q are the deprojected baselines.

These visibilities (right-hand side of Equation (A1)) are sampled at the same *uv*-coverage of each data set, and then, we use FRANKENSTEIN to fit them (using the same methodology and hyperparameters described in Table 3) and try to retrieve the delta function's input brightness distribution. FRANKENSTEIN reconstructs a Gaussian function instead of a delta function, with FWHM that depends on the *uv*-coverage. This FWHM represents the minimum spatial scale recoverable by the visibility fit, i.e., the intrinsic angular resolution of the visibility fit. A Gaussian function is fitted to the reconstructed brightness profile, and the FWHM is reported in the last column in Table 3. We remark that this methodology is equivalent to the definition of the PSF, defined as the response of an imaging system (e.g., an interferometer) to a point source. Deconvolution and imaging software (e.g., CASA) fits the 2D intensity distribution of the PSF to quantify the minimum recoverable spatial scale for a given *uv*-coverage, in an analogous way to our constraint of the spatial scale that our method recovers when the source is an infinitely narrow ring.

[14] Note that $R_{\rm max}$ is not a rigorous measurement of the disk radius but rather the maximum radial extent in the visibility fit. As suggested by J. Jennings et al. (2020), a suitable choice for $R_{\rm max}$ is typically greater than 1.5 times the expected disk radius.

A.2. Gaussian Disk

As a second method to infer the intrinsic angular resolution, we compute the visibilities of a full Gaussian disk of a certain FWHM (Θ) at the same *uv*-coverage of each observation. The visibilities are computed using the Hankel transform of a Gaussian disk as

$$\mathcal{H}\left[\frac{1}{\Theta}\sqrt{\frac{4\ln 2}{\pi}}\exp\left(-\frac{4\ln 2 r^2}{\Theta^2}\right)\right] = \exp\left(-\frac{(\pi\Theta q)^2}{4\ln 2}\right). \quad \text{(A2)}$$

Then, these visibilities are fitted with FRANKENSTEIN, where a Gaussian function similar to that of the input model is obtained. The comparison between the input FWHM and that obtained with FRANKENSTEIN is shown in the left panel of Figure 7 for the *uv*-coverage of LkCa15 at Band 6 and 9. Note that the FWHM obtained with FRANKENSTEIN differs from the input value when the latter tends to be zero. The horizontal dashed lines are the angular resolutions computed from the delta rings in the previous section. These values represent the minimum spatial scale that a FRANKENSTEIN fit with a certain *uv*-coverage is able to resolve.

A.3. The Effects of Thermal Noise When Resolving Two Delta Rings

The input models for a delta ring and Gaussian disk above were computed without including thermal noise to the visibilities. In this section, we demonstrate that our visibility fit resolves the emission of two delta rings, with or without the inclusion of thermal noise. The first input model consists of two delta rings separated by 50 mas around $R_{\rm max}/2 = 1.''1$. The visibilities of each delta ring are sampled at the *uv*-coverage of LkCa15 at Band 6 using the Equation (A1). The second model is the same but including thermal noise to the visibilities. The thermal noise is simulated by randomly choosing a visibility measurement within the visibilities' error bar at each baseline. Then, we use FRANKENSTEIN in both models to reconstruct the brightness radial profile. The visibility fit to the mock data is shown in the middle panel of Figure 7, and the reconstructed radial profiles are shown in the right panel of the same Figure. In both cases, the visibility fit is able to resolve both rings, with an FWHM of 21.5 mas, as already computed in Sections A.1–A.2.

Appendix B
More on Visibility Modeling

B.1. Best Models and Residuals

The visibility models presented in Figure 2 are used to generate synthetic observations of the disks. Each model is sampled with the same *uv*-coverage as the observations and then imaged with identical observational parameters as described in Table 2. Figure 8 shows the CLEAN images of the disk models for all the observations.

On the other hand, the visibility residuals (data, model) are computed and also used to generate synthetic observations. After sampling the visibility residuals with the same *uv*-coverage as the observations, they are imaged and shown in Figure 9. Each map is normalized to the rms of each observation. The red/blue areas indicate regions with excess/deficit emission relative to the azimuthally averaged intensity of each observation.

B.2. Parametric Models at VLA Wavelengths

The parametric models for VLA data are given by a sum of Gaussian functions and a delta function $\delta(r)$ (mimic the compact emission from free–free) at the disk center:

$$I(r) = \sum_i A_i \exp\left[-\frac{(r-r_i)^2}{2\sigma_i^2}\right] + f_0\,\delta(r). \quad \text{(B1)}$$

The number of Gaussian functions for each disk is chosen based on the radial profile at ALMA wavelengths. The radial positions (r_i) of the Gaussian functions are fixed in all cases, determined by the ring locations observed at longer ALMA wavelengths for each respective disk. We also conducted tests allowing r_i to be a free parameter, and the resulting posterior probability distributions aligned with those when the radial positions were fixed. Therefore, to mitigate the ambiguity between the remaining free parameters, we opted to keep the radial positions of the Gaussian functions fixed.

The free parameters (A_i, σ_i, f_0) are determined via an MCMC method (implemented in the Python library EMCEE, D. Foreman-Mackey et al. 2013), aiming to minimize the logarithm of the likelihood function given by Equation (2), and using 64 walkers and 10,000 steps. Table 5 shows the parametric model chosen for each disk and the best fit for each parameter. Low and upper error bars correspond to percentiles 16 and 84, respectively.

The free–free flux (last column) for LkCa15, RXJ1615, and SR24S is 17.8, 44.7, and 11.0 μJy respectively. These values are high compared with the rest of the disks in this work. L. A. Zapata et al. (2017) showed that the SED of these disks can be described as a two-component power law: one of them associated with thermal dust emission, and the other to free–free emission, consistent with our estimations. Meanwhile, they claim that, for UXTau A, a single power law (from optically thin dust emission) is enough to reproduce the SED. Our free–free flux estimation for UXTau A is only 0.05 μJy, which is below the sensitivity (14.9 μJy), and thus, it is not detected in this work. For DMTau, the best fit is consistent with a low free–free flux of only 0.02 μJy, which is a nondetection given the sensitivity of 9 μJy. No free–free emission was detected in L. A. Zapata et al. (2017) in DMTau either. However, it is known that the free–free from ionized gas is variable Y. Terada et al. (2023). Finally, the free–free emission of CQ Tau is also

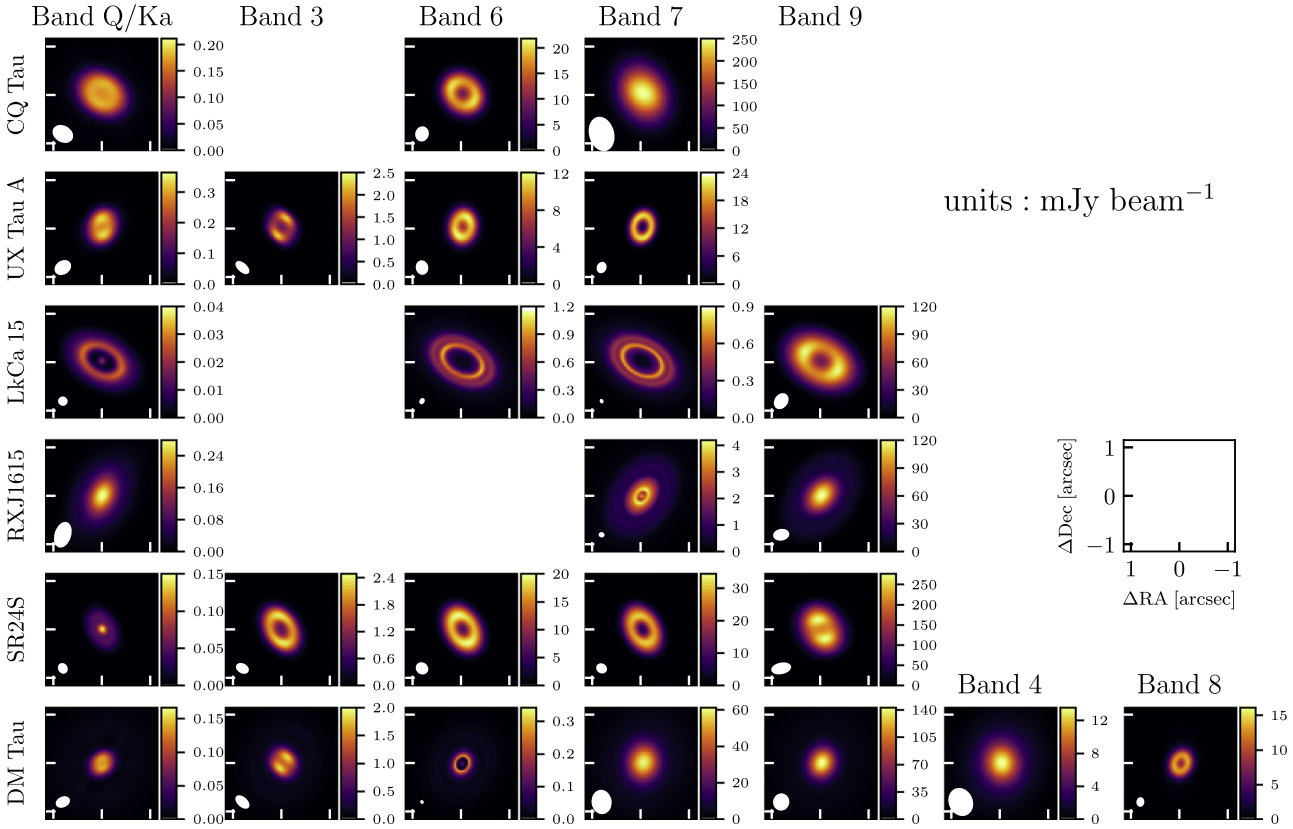

Figure 8. CLEAN images of the disk models in our sample. The color bars are the same as in Figure 1.

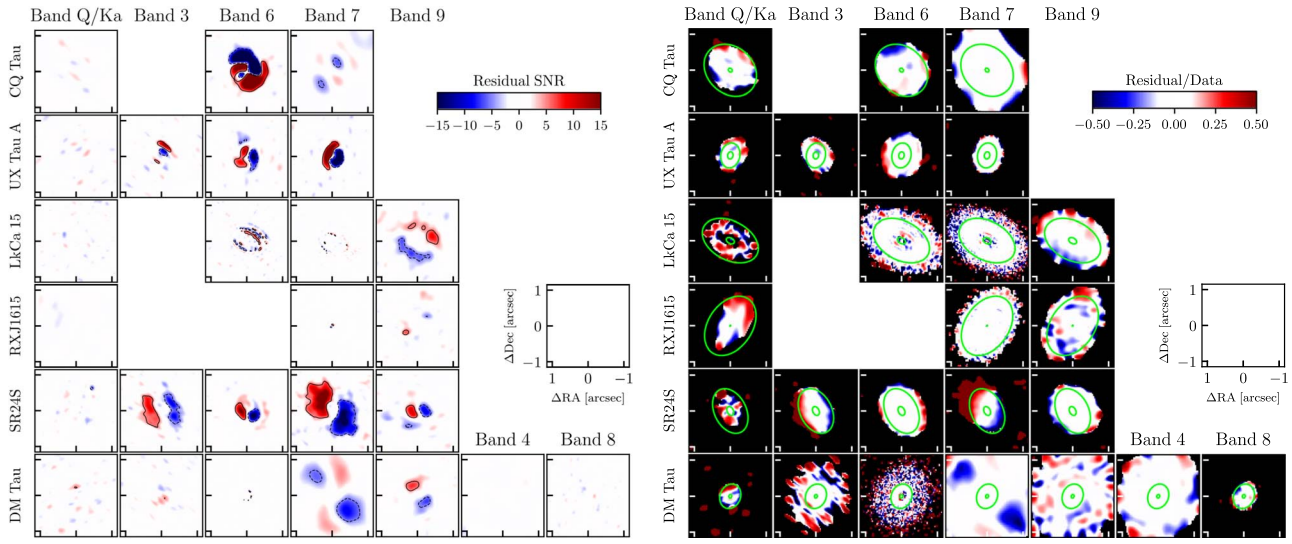

Figure 9. Residual maps normalized with the rms (left) and the intensity maps (right). The name and band of the disk are shown in the top left and top right corner of each panel, respectively. The solid/dashed contours in the left figure are the region with a signal-to-noise ratio (SNR) of +5/−5, respectively. The black area in the right figure is the region where the intensity map has an SNR <3. The green ellipses show the minimum and maximum radius where dust properties' constraints are computed in Figure 5.

Table 5
Best Fits of the Parametric Model for VLA Observations

Source	Parametric Model	$\log_{10}(A_0)$ (Jy sr^{-1})	Fixed r_0 (arcsec)	$\log_{10}(\sigma_0)$ (arcsec)	$\log_{10}(A_1)$ (Jy sr^{-1})	Fixed r_1 (arcsec)	$\log_{10}(\sigma_1)$ (arcsec)	$\log_{10}(f_0)$ (Jy)
CQTau	1 Gaussian + point source	$7.83^{+0.02}_{-0.02}$	0.300	$-0.92^{+0.02}_{-0.02}$	⋯	⋯	⋯	$-6.29^{+1.05}_{-1.14}$
UXTau A	1 Gaussian + point source	$8.43^{+0.06}_{-0.05}$	0.236	$-1.26^{+0.06}_{-0.07}$	⋯	⋯	⋯	$-7.31^{+1.85}_{-1.83}$
LkCa15	2 Gaussians + point source	$7.56^{+0.06}_{-0.06}$	0.433	$-1.21^{+0.07}_{-0.07}$	$7.08^{+0.05}_{-0.06}$	0.635	$-0.81^{+0.06}_{-0.06}$	$-4.75^{+0.10}_{-0.12}$
RXJ1615	2 Gaussians + point source	$7.78^{+0.08}_{-0.08}$	0.158	$-0.85^{+0.07}_{-0.09}$	$7.52^{+1.09}_{-0.62}$	$0.73^{+0.05}_{-0.08}$	$-1.72^{+0.90}_{-1.18}$	$-4.35^{+0.17}_{-0.29}$
SR24S	2 Gaussian + point source	$7.74^{+0.11}_{-0.06}$	0.254	$-1.00^{+0.13}_{-0.21}$	$7.42^{+1.25}_{-1.43}$	0.441	$-1.83^{+0.73}_{-0.77}$	$-4.96^{+0.85}_{-0.97}$
DMTau	2 Gaussian + point source	$8.26^{+0.12}_{-0.08}$	0.180	$-1.36^{+0.08}_{-0.13}$	$6.57^{+0.53}_{-0.25}$	0.860	$-0.83^{+0.38}_{-0.66}$	$-7.57^{+1.92}_{-1.68}$

low and below the sensitivity (7 μJy). The nondetection of free–free emission is consistent with the lack of detection at 3.6 and 6.0 cm, suggesting that the flux at 7 mm is dominated by dust thermal emission (L. Testi et al. 2001).

Appendix C
Radial Smearing Effects

The inferred dust properties depend on the lowest angular resolution of the multiwavelength data. Higher contrasts between rings and gaps are expected in future high angular resolution observations. Radial smearing effects could potentially influence the inferred dust property profiles. For instance, optically thick emission at the rings could smear into the cavity region. This could mimic faint dust continuum emission with low spectral indices within the cavity, which might be attributed to large grain sizes (similar to those in CQTau, SR24, and DMTau).

It is important to note that our methodology for studying the dust properties' radial profiles cannot directly infer the deconvolved or convolved dust properties' radial profiles. Instead, it provides only an approximation of those values, depending on the angular resolution. For example, in the optically thin regime and Rayleigh–Jeans approximation, the emergent intensity is the product of three free parameters: $I_\nu \propto T_{\rm d}\Sigma_{\rm d}\kappa_\nu$. Since we observe the convolved intensities $\mathcal{C}(I_\nu)$, we can only infer the convolution of the product of the three free parameters, rather than the product of individual convolved profiles $\mathcal{C}(T_{\rm d}\Sigma_{\rm d}\kappa_\nu) \neq \mathcal{C}(T_{\rm d}) \times \mathcal{C}(\Sigma_{\rm d}) \times \mathcal{C}(\kappa_\nu)$. We only have good approximations to the convolved dust properties' radial profiles when the angular resolution is sufficiently high (Viscardi et al. in prep).

We study the effects of radial smearing by creating a disk model with properties similar to those of DMTau, where large grain sizes are inferred within the disk cavity. The temperature radial profile model is computed from a passively irradiated disk and the DMTau stellar parameters (Table 1). The maximum grain size model is given by $0.1(r/0\farcs2)^{-0.5} + \exp[-0.5((r - 0\farcs2)/0\farcs015)^2]$ cm, and the dust surface density is given by $0.01 + \exp(-0.5(r - 0.2'')^2/\sigma^2)$ g cm^{-2}, with $\sigma = 0\farcs02$, for $r > 0\farcs2$ and $\sigma = 0\farcs005$ for $r \leqslant 0\farcs2$ to mimic an asymmetric ring. These radial profiles, chosen to represent dust trap signatures, are shown as a solid curve in the left panels of Figure 10. The dashed lines in the same panels are the convolved radial profiles, using the resolution of the DMTau observations (120 mas). The middle panels show the convolved intensity profiles (top) and optical depths (bottom) corresponding to the same multiwavelength observation as DMTau. The intensities and optical depths were originally computed using the dust

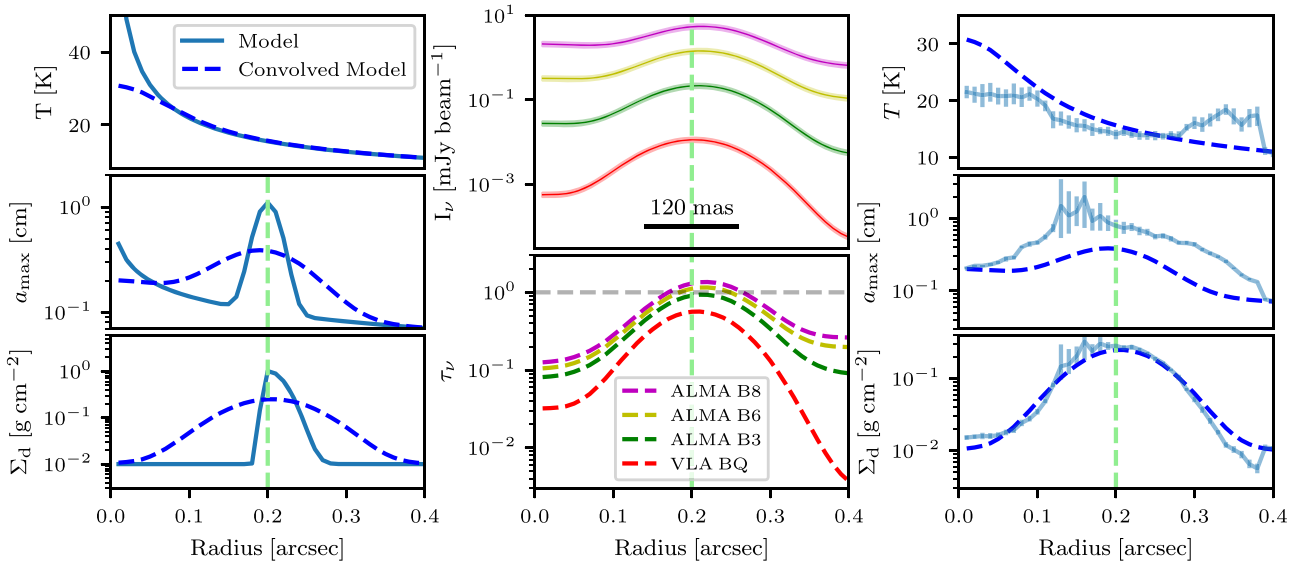

Figure 10. Left panels: dust temperature, maximum grain size and dust surface density (from top to bottom) radial profile models (solid lines), and convolved profiles (dashed lines) with a 120 mas beam size (DMTau angular resolution). Middle panels: intensity radial profiles (top) and optical depths (bottom) at the same resolution and multifrequency observations as DMTau. Right panels: dust temperature, maximum grain size, and dust surface density (from top to bottom) best fits (error bars), and input models (dashed lines).

properties models, and then, these profiles were convolved to the same angular resolution.

The right panels show the best fit for dust temperature (top), maximum grain size (middle), and dust surface density (bottom). The blue dashed lines are the convolved radial profiles shown in the left panels. Any discrepancy between the radial profile from the posterior probability and the convolved radial profiles is due to the inability to independently infer the convolved dust properties' radial profiles from observations (radial smearing effects), as discussed above. Note that the temperature and dust surface density radial profiles are well reproduced. However, the maximum grain size around the peak is radially smeared (much beyond the convolved radial profile), mimicking large grain sizes within the cavity, similar to the dust properties inferred in SR24S and DMTau (Figure 5). Thus, although large grain sizes within the cavity can reproduce the intensity profiles for CQTau, SR24S, and DMTau, we cannot rule out the possibility of small grain sizes in this region, which are hidden by radial smearing effects.

ORCID iDs

Anibal Sierra https://orcid.org/0000-0002-5991-8073
Laura M. Pérez https://orcid.org/0000-0002-1199-9564
Benjamín Sotomayor https://orcid.org/0009-0009-9182-3240
Myriam Benisty https://orcid.org/0000-0002-7695-7605
Claire J. Chandler https://orcid.org/0000-0002-7570-5596
Sean Andrews https://orcid.org/0000-0003-2253-2270
John Carpenter https://orcid.org/0000-0003-2251-0602
Thomas Henning https://orcid.org/0000-0002-1493-300X
Leonardo Testi https://orcid.org/0000-0003-1859-3070
Luca Ricci https://orcid.org/0000-0001-8123-2943
David Wilner https://orcid.org/0000-0003-1526-7587

References

Alexander, R. D., Clarke, C. J., & Pringle, J. E. 2006, MNRAS, 369, 229
Andrews, S. M., Chandler, C. J., Isella, A., et al. 2014, ApJ, 787, 148
Andrews, S. M., Elder, W., Zhang, S., et al. 2021, ApJ, 916, 51
Andrews, S. M., Wilner, D. J., Espaillat, C., et al. 2011, ApJ, 732, 42
Andrews, S. M., Wilner, D. J., Hughes, A. M., Qi, C., & Dullemond, C. P. 2009, ApJ, 700, 1502
Artymowicz, P., & Lubow, S. H. 1996, ApJL, 467, L77
Asensio-Torres, R., Henning, T., Cantalloube, F., et al. 2021, A&A, 652, A101
Astropy Collaboration, Price-Whelan, A. M., Sipőcz, B. M., et al. 2018, AJ, 156, 123
Astropy Collaboration, Robitaille, T. P., Tollerud, E. J., et al. 2013, A&A, 558, A33
Avenhaus, H., Quanz, S. P., Garufi, A., et al. 2018, ApJ, 863, 44
Balbus, S. A., & Hawley, J. F. 1991, ApJ, 376, 214
Benisty, M., Bae, J., Facchini, S., et al. 2021, ApJL, 916, L2
Birnstiel, T., Andrews, S. M., & Ercolano, B. 2012a, A&A, 544, A79
Birnstiel, T., Dullemond, C. P., Zhu, Z., et al. 2018, ApJL, 869, L45
Birnstiel, T., Fang, M., & Johansen, A. 2016, SSRv, 205, 41
Birnstiel, T., Klahr, H., & Ercolano, B. 2012b, A&A, 539, A148
Ribas, Á., Bouy, H., & Merín, B. 2015, A&A, 576, A52
Brown, J. M., Blake, G. A., Dullemond, C. P., et al. 2007, ApJL, 664, L107
Brown, J. M., Blake, G. A., Qi, C., et al. 2009, ApJ, 704, 496
Calvet, N., D'Alessio, P., Hartmann, L., et al. 2002, ApJ, 568, 1008
Carrasco-González, C., Sierra, A., Flock, M., et al. 2019, ApJ, 883, 71
Casassus, S., van der Plas, G. M., Perez, S., et al. 2013, Natur, 493, 191
Christiaens, V., Samland, M., Henning, T., et al. 2024, A&A, 685, L1
Cieza, L. A., González-Ruilova, C., Hales, A. S., et al. 2021, MNRAS, 501, 2934
Delussu, L., Birnstiel, T., Miotello, A., et al. 2024, A&A, 688, A81
Dong, R., Zhu, Z., & Whitney, B. 2015, ApJ, 809, 93
Draine, B. T. 2006, ApJ, 636, 1114
Drkažkowska, J., Bitsch, B., Lambrechts, M., et al. 2023, in ASP Conf. Ser. 534, Protostars and Planets VII, ed. S. Inutsuka et al. (San Francisco, CA: ASP), 717
Dubrulle, B., Morfill, G., & Sterzik, M. 1995, Icar, 114, 237
Dullemond, C. P., Dominik, C., & Natta, A. 2001, ApJ, 560, 957
Espaillat, C., D'Alessio, P., Hernández, J., et al. 2010, ApJ, 717, 441
Facchini, S., Benisty, M., Bae, J., et al. 2020, A&A, 639, A121
Flock, M., Ruge, J. P., Dzyurkevich, N., et al. 2015, A&A, 574, A68
Foreman-Mackey, D., Hogg, D. W., Lang, D., & Goodman, J. 2013, PASP, 125, 306
Francis, L., & van der Marel, N. 2020, ApJ, 892, 111
Gaia Collaboration 2020, yCat, 1350, 0
Gárate, M., Delage, T. N., Stadler, J., et al. 2021, A&A, 655, A18
Goldreich, P., & Tremaine, S. 1979, ApJ, 233, 857
Harris, C. R., Millman, K. J., van der Walt, S. J., et al. 2020, Natur, 585, 357
Hartmann, L., Herczeg, G., & Calvet, N. 2016, ARA&A, 54, 135
Hashimoto, J., Muto, T., Dong, R., et al. 2021, ApJ, 911, 5
Hayashi, C. 1981, PThPS, 70, 35

Hoang, T., Lan, N.-Q., Vinh, N.-A., & Kim, Y.-J. 2018, ApJ, 862, 116
Huang, J., Andrews, S. M., Dullemond, C. P., et al. 2018, ApJL, 869, L42
Hull, C. L. H., Yang, H., Li, Z.-Y., et al. 2018, ApJ, 860, 82
Hunter, J. D. 2007, CSE, 9, 90
Isella, A., Andrews, S. M., Dullemond, C. P., et al. 2019a, LPSC, 50, 2821
Isella, A., Benisty, M., Teague, R., et al. 2019b, ApJL, 879, L25
Isella, A., Chandler, C. J., Carpenter, J. M., Pérez, L. M., & Ricci, L. 2014, ApJ, 788, 129
Jennings, J., Booth, R. A., Tazzari, M., Rosotti, G. P., & Clarke, C. J. 2020, MNRAS, 495, 3209
Jennings, J., Booth, R. A., Tazzari, M., Clarke, C. J., & Rosotti, G. P. 2022, MNRAS, 509, 2780
Kataoka, A., Muto, T., Momose, M., Tsukagoshi, T., & Dullemond, C. P. 2016a, ApJ, 820, 54
Kataoka, A., Tsukagoshi, T., Momose, M., et al. 2016b, ApJL, 831, L12
Klahr, H. H., & Henning, T. 1997, Icar, 128, 213
Konigl, A., & Pudritz, R. E. 2000, in Protostars and Planets IV, ed. V. Mannings, A. P. Boss, & S. S. Russell (Tucson, AZ: Univ. Arizona Press), 759
Kraus, A. L., & Ireland, M. J. 2012, ApJ, 745, 5
Kraus, A. L., Ireland, M. J., Martinache, F., & Hillenbrand, L. A. 2011, ApJ, 731, 8
Kudo, T., Hashimoto, J., Muto, T., et al. 2018, ApJL, 868, L5
Lin, D. N. C., & Papaloizou, J. 1979, MNRAS, 186, 799
Lin, Z.-Y. D., Li, Z.-Y., Stephens, I. W., et al. 2024, MNRAS, 528, 843
Lin, Z.-Y. D., Li, Z.-Y., Yang, H., et al. 2023, MNRAS, 520, 1210
Liu, H. B. 2019, ApJL, 877, L22
Liu, H. B., Muto, T., Konishi, M., et al. 2024, A&A, 685, A18
Liu, Y., Henning, T., Carrasco-González, C., et al. 2017, A&A, 607, A74
Lodato, G., Dipierro, G., Ragusa, E., et al. 2019, MNRAS, 486, 453
Long, F., Andrews, S. M., Zhang, S., et al. 2022, ApJL, 937, L1
Macías, E., Espaillat, C. C., Ribas, Á., et al. 2018, ApJ, 865, 37
Macías, E., Guerra-Alvarado, O., Carrasco-González, C., et al. 2021, A&A, 648, A33
Manara, C. F., Testi, L., Natta, A., et al. 2014, A&A, 568, A18
Maucó, K., Carrasco-González, C., Schreiber, M. R., et al. 2021, ApJ, 923, 128
McMullin, J. P., Waters, B., Schiebel, D., Young, W., & Golap, K. 2007, in ASP Conf. Ser. 376, Astronomical Data Analysis Software and Systems XVI, ed. R. A. Shaw, F. Hill, & D. J. Bell (San Francisco, CA: ASP), 127
Mori, T., Kataoka, A., Ohashi, S., et al. 2019, ApJ, 883, 16
Mouillet, D., Lagrange, A. M., Augereau, J. C., & Ménard, F. 2001, A&A, 372, L61
Muto, T., Grady, C. A., Hashimoto, J., et al. 2012, ApJL, 748, L22
Natta, A., Testi, L., & Randich, S. 2006, A&A, 452, 245
Paneque-Carreño, T., Pérez, L. M., Benisty, M., et al. 2021, ApJ, 914, 88
Pascucci, I., Cabrit, S., Edwards, S., et al. 2023, in ASP Conf. Ser. 534, Protostars and Planets VII, ed. S. Inutsuka et al. (San Francisco, CA : ASP), 567
Pearson, T. J. 1999, in ASP Conf. Ser. 180, Synthesis Imaging in Radio Astronomy II, ed. G. B. Taylor, C. L. Carilli, & R. A. Perley (San Francisco, CA: ASP), 335
Pérez, L. M., Carpenter, J. M., Andrews, S. M., et al. 2016, Sci, 353, 1519
Pérez, L. M., Carpenter, J. M., Chandler, C. J., et al. 2012, ApJL, 760, L17
Pérez, L. M., Chandler, C. J., Isella, A., et al. 2015, ApJ, 813, 41
Pérez, L. M., Isella, A., Carpenter, J. M., & Chandler, C. J. 2014, ApJL, 783, L13
Pinilla, P., Benisty, M., & Birnstiel, T. 2012a, A&A, 545, A81
Pinilla, P., Benisty, M., Birnstiel, T., et al. 2014, A&A, 564, A51
Pinilla, P., Birnstiel, T., Ricci, L., et al. 2012b, A&A, 538, A114
Pinilla, P., Flock, M., Ovelar, M. d. J., & Birnstiel, T. 2016, A&A, 596, A81
Pinilla, P., Pascucci, I., & Marino, S. 2020, A&A, 635, A105
Pinilla, P., Pérez, L. M., Andrews, S., et al. 2017, ApJ, 839, 99
Pinilla, P., Tazzari, M., Pascucci, I., et al. 2018, ApJ, 859, 32
Regály, Z., Juhász, A., Sándor, Z., & Dullemond, C. P. 2012, MNRAS, 419, 1701
Rich, E. A., Teague, R., Monnier, J. D., et al. 2021, ApJ, 913, 138
Rilinger, A. M., Espaillat, C. C., Xin, Z., et al. 2023, ApJ, 944, 66
Robert, C. M. T., Méheut, H., & Ménard, F. 2020, A&A, 641, A128
Schräpler, R., & Henning, T. 2004, ApJ, 614, 960
Semenov, D., Favre, C., Fedele, D., et al. 2018, A&A, 617, A28
Sierra, A., & Lizano, S. 2020, ApJ, 892, 136
Sierra, A., Lizano, S., Macías, E., et al. 2019, ApJ, 876, 7
Sierra, A., Pérez, L. M., Zhang, K., et al. 2021, ApJS, 257, 14
Strom, K. M., Strom, S. E., Edwards, S., Cabrit, S., & Skrutskie, M. F. 1989, AJ, 97, 1451
Takeuchi, T., & Lin, D. N. C. 2002, ApJ, 581, 1344
Tazaki, R., Tanaka, H., Kataoka, A., Okuzumi, S., & Muto, T. 2019, ApJ, 885, 52
Tazzari, M. 2017, mtazzari/uvplot v3.1, Zenodo, doi: 10.5281/zenodo.1003113
Teague, R. 2019, JOSS, 4, 1632
Terada, Y., Liu, H. B., Mkrtichian, D., et al. 2023, ApJ, 953, 147
Testi, L., Birnstiel, T., Ricci, L., et al. 2014, in Protostars and Planets VI, ed. H. Beuther et al. (Tucson, AZ: Univ. Arizona Press), 339
Testi, L., Natta, A., Shepherd, D. S., & Wilner, D. J. 2001, ApJ, 554, 1087
Thompson, A. R., Moran, J. M., & Swenson, G. W. J. 2017, Interferometry and Synthesis in Radio Astronomy (3rd edn; Berlin: Springer)
Toomre, A. 1964, ApJ, 139, 1217
Ubeira Gabellini, M. G., Miotello, A., Facchini, S., et al. 2019, MNRAS, 486, 4638
Ueda, T., Kataoka, A., & Tsukagoshi, T. 2020, ApJ, 893, 125
van der Marel, N. 2023, EPJP, 138, 225
van der Marel, N., Birnstiel, T., Garufi, A., et al. 2021, AJ, 161, 33
van der Marel, N., van Dishoeck, E. F., Bruderer, S., Pérez, L., & Isella, A. 2015, A&A, 579, A106
van der Marel, N., van Dishoeck, E. F., Bruderer, S., et al. 2016, A&A, 585, A58
Varga, J., Hogerheijde, M., van Boekel, R., et al. 2021, A&A, 647, A56
Wahhaj, Z., Cieza, L., Koerner, D. W., et al. 2010, ApJ, 724, 835
Weidenschilling, S. J. 1977, MNRAS, 180, 57
Whipple, F. L. 1972, in From Plasma to Planet, ed. A. Elvius (New York: Wiley), 211
Wölfer, L., Facchini, S., van der Marel, N., et al. 2023, A&A, 670, A154
Yang, H., Fernández-López, M., Li, Z.-Y., et al. 2024, ApJ, 963, 134
Yang, H., Li, Z.-Y., Looney, L., & Stephens, I. 2016, MNRAS, 456, 2794
Zapata, L. A., Rodríguez, L. F., & Palau, A. 2017, ApJ, 834, 138
Zhang, S., Zhu, Z., Ueda, T., et al. 2023, ApJ, 953, 96
Zhu, Z., Zhang, S., Jiang, Y.-F., et al. 2019, ApJL, 877, L18
Zurlo, A., Cugno, G., Montesinos, M., et al. 2020, A&A, 633, A119